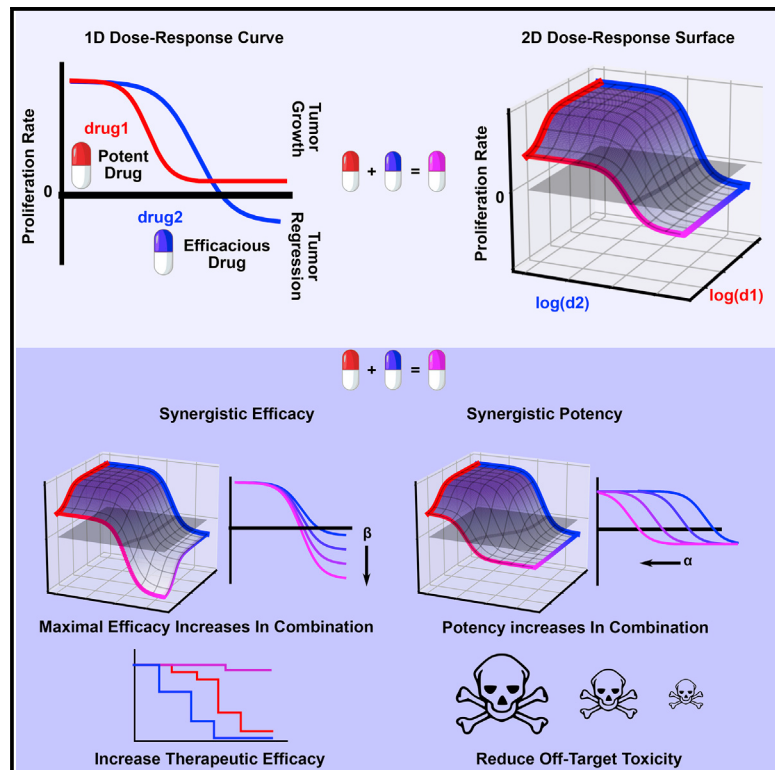


Cell Systems

Quantifying Drug Combination Synergy along Potency and Efficacy Axes

Graphical Abstract



Highlights

- MuSyC is a synergy framework applicable to any metric of drug combination effect
- Unlike other methods, MuSyC decouples synergy of potency and efficacy
- It subsumes traditional synergy methods, resolving ambiguities and biases in the field
- MuSyC reveals optimal co-targeting strategies in NCSLC and melanoma

Authors

Christian T. Meyer, David J. Wooten, B. Bishal Paudel, ..., Leonard A. Harris, Darren R. Tyson, Vito Quaranta

Correspondence

vito.quaranta@vanderbilt.edu

In Brief

Meyer et al. developed a framework for measuring drug combination synergy. The framework, termed MuSyC, distinguishes between two types of synergy. The first quantifies the change in the maximal effect with the combination (synergistic efficacy), and the second measures the change in a drug's potency due to the combination (synergistic potency). By decoupling these two synergies conflated in prior methods, MuSyC rationally guides discovery and translation of drug combinations for the improvement of therapeutic efficacy and reduction of off-target toxicities via dose reduction.



Quantifying Drug Combination Synergy along Potency and Efficacy Axes

Christian T. Meyer,^{1,3,9} David J. Wooten,^{2,3,9} B. Bishal Paudel,^{4,5,9} Joshua Bauer,^{4,5,6} Keisha N. Hardeman,^{4,5} David Westover,⁶ Christine M. Lovly,^{5,7} Leonard A. Harris,^{3,4} Darren R. Tyson,^{3,4} and Vito Quaranta^{3,4,8,10,*}

¹Program in Chemical and Physical Biology, Vanderbilt University School of Medicine, Nashville, TN 37232, USA

²Program in Cancer Biology, Vanderbilt University School of Medicine, Nashville, TN 37232, USA

³Center for Cancer Systems Biology at Vanderbilt, Vanderbilt University, Nashville, TN 37232, USA

⁴Department of Biochemistry, Vanderbilt University, Nashville, TN 37232, USA

⁵Vanderbilt Ingram Cancer Center, Vanderbilt University Medical Center, Nashville, TN 37232, USA

⁶Institute of Chemical Biology, High-Throughput Screening Facility, Vanderbilt University, Nashville, TN 37232, USA

⁷Department of Medicine, Division of Hematology and Oncology, Vanderbilt University Medical Center, Nashville, TN 37232, USA

⁸Department of Pharmacology, Vanderbilt University School of Medicine, Nashville, TN 37232, USA

⁹These authors contributed equally

¹⁰Lead Contact

*Correspondence: vito.quaranta@vanderbilt.edu

<https://doi.org/10.1016/j.cels.2019.01.003>

SUMMARY

Two goals motivate treating diseases with drug combinations: reduce off-target toxicity by minimizing doses (synergistic potency) and improve outcomes by escalating effect (synergistic efficacy). Established drug synergy frameworks obscure such distinction, failing to harness the potential of modern chemical libraries. We therefore developed multi-dimensional synergy of combinations (MuSyC), a formalism based on a generalized, multi-dimensional Hill equation, which decouples synergistic potency and efficacy. In mutant-EGFR-driven lung cancer, MuSyC reveals that combining a mutant-EGFR inhibitor with inhibitors of other kinases may result only in synergistic potency, whereas synergistic efficacy can be achieved by co-targeting mutant-EGFR and epigenetic regulation or microtubule polymerization. In mutant-BRAF melanoma, MuSyC determines whether a molecular correlate of BRAFi insensitivity alters a BRAF inhibitor's potency, efficacy, or both. These findings showcase MuSyC's potential to transform the enterprise of drug-combination screens by precisely guiding translation of combinations toward dose reduction, improved efficacy, or both.

INTRODUCTION

Recent decades have witnessed an exponential expansion of available drugs for the treatment of diseases (Gong et al., 2017). This expansion has been concomitant with an evolving understanding of disease complexity—complexity commonly necessitating combination therapy (He et al., 2016). However, clinical applications of combination therapy are often limited by tolerable dose ranges, and, therefore, it is desirable to identify

combinations that enable dose reduction (Tallarida, 2011), i.e., synergistic potency. Additionally, combining drugs does not guarantee *a priori* an increase in efficacy over the single agents, and, therefore, it is desirable to identify combinations with effects greater than what is achievable with either drug alone (Fouquerier and Guedj, 2015), i.e., synergistic efficacy. To assess a combination's performance toward these goals, several drug synergy metrics have been proposed (Fouquerier and Guedj, 2015). The roots of current synergy metrics can be traced back to either Loewe, who advanced the dose additivity principle (Loewe and Muischnek, 1926) or Bliss who first described the multiplicative survival principle (Bliss, 1939). Nearly a century later, methods to quantify drug synergy continue to appear (Chou, and Talalay, 1983; Yadav et al., 2015; Twarog et al., 2016; Zimmer et al., 2016; Schindler, 2017) based on these two principles. However, none of these methods distinguish between synergistic potency and synergistic efficacy. Instead, they either make no distinction or tacitly assume the only form of synergism is through potency.

Nevertheless, this distinction is essential to arrive at an unambiguous definition of synergy and properly rationalize the deployment of drug combinations, e.g., in personalized medicine. Indeed, conflating them may mislead drug combination discovery efforts. For instance, a search for improved efficacy based on traditional synergy frameworks may be confounded by an inability to sort out synergistically potent combinations.

To address this critical shortcoming and resolve these two independent types of synergy, herein we propose a synergy framework termed multi-dimensional synergy of combinations (MuSyC), which is based on a two-dimensional (2D) extension of the Hill equation derived from mass action kinetics. The 2D Hill equation extends dose-response curves to dose-response surfaces.

MuSyC distinguishes between synergistic potency and synergistic efficacy based on parameters in the 2D Hill equation. These synergy parameters are extensions of standard pharmacologic measures of potency and efficacy and define a dose-response surface onto which changes in potency and efficacy



Table 1. Key Definitions

Potency	The amount of drug required to produce a specified effect. A highly potent drug is active at low concentrations. Classically quantified as the required concentration to achieve half the maximal effect (EC50).
Efficacy	The degree to which a drug can produce a beneficial effect. Classically quantified as the maximal effect (E_{max}).
Synergistic potency	The magnitude of the change in the drug potency, owing to the presence of another drug.
Synergistic efficacy	The percent change in the maximal efficacy of the combination compared to the most efficacious single agent.

are orthogonal. We visualize synergy of potency and efficacy on drug synergy diagrams (DSDs), which globally stratify drug combinations along orthogonal axes of synergy facilitating comparisons between the synergistic profiles of many combinations.

To demonstrate the value of MuSyC, we investigate a panel of anti-cancer compounds in combination with a third-generation mutant-EGFR inhibitor, osimertinib, in EGFR-mutant non-small-cell lung cancer (NSCLC). We find that drugs targeting epigenetic regulators or microtubule polymerization are synergistically efficacious with osimertinib. In contrast, drugs co-targeting kinases in the MAPK pathway affect potency, not efficacy of osimertinib. These conclusions have implications for drug combination deployment in NSCLC where increasing the efficacy of EGFR inhibitors has historically relied on trial and error, with no overarching principles to guide development (Schiffmann et al., 2016).

We also apply MuSyC to study the well-established, clinically relevant combination targeting RAF and MEK in BRAF-mutant melanoma (Long et al., 2014). We find this combination to be synergistically efficacious, though, in several cases, at the cost of potency. We then identify NADPH oxidase 5 (NOX5) as a previously unsuspected molecular determinant of sensitivity to BRAF inhibition (BRAFi) in BRAF-mutant melanoma. Applying MuSyC, we find that NOX5 expression levels affect BRAFi efficacy but not potency.

In direct comparisons, we found that traditional synergy frameworks are biased and ambiguous even for the most synergistically efficacious of the NSCLC and melanoma combination studies, leading to misclassifications of combination synergy. We further show how MuSyC addresses and corrects these problems by generalizing the traditional models.

RESULTS

2D Hill Equation Decouples Synergy of Efficacy from Synergy of Potency

The dose-effect relationship of a single drug is traditionally quantified by the Hill equation, which contains parameters describing efficacy (E_{max}) and potency (EC50) of a dose-response curve (see STAR Methods for equation derivation; Table 1 for definitions) (Figure 1A). The Hill equation is derived from a phenomenological 2-state model of drug effect (Figure S1A). Therefore,

to characterize the dose-effect relationship for drug combinations, we extended this model to a 4-state model (Figure S1B) to derive a 2D generalization of the Hill equation, using principles of mass action kinetics (see STAR Methods). The 2D Hill equation parameterizes a dose-response surface (Figure 1B; Table S1 for parameter descriptions) (Greco et al., 1995), a 2D extension of 1D dose-response curves (Figure 1A). In this equation, the changes in the efficacy and potency resulting from the combination are quantified by parameters for synergistic efficacy, denoted by β , and synergistic potency, denoted by α (Table S1). These parameters govern the shape of the dose-response surface and can capture complex patterns in experimental data.

The parameter β is defined as the percent increase in a drug combination's effect beyond the most efficacious single drug. For instance, in the case of synergistic efficacy ($\beta > 0$), the effect at the maximum concentration of both drugs ($E3$) exceeds the maximum effect of either drug alone ($E1$ or $E2$) (Figure 1C, quadrants I and II). For antagonistic efficacy ($\beta < 0$) (Figure 1C, quadrants III and IV), at least one or both drugs are more efficacious as single agents than in combination (see Video S1 for an animated example of how the dose-response surface changes as a function of β).

The parameter α quantifies how the effective dose of one drug is altered by the presence of the other. In the case of synergistic potency ($\alpha > 1$), the EC50 (denoted C in Figure 1B) decreases because of the addition of the other drug (Figure 1C, quadrants I and IV), corresponding to an increase in potency. In the case of antagonistic potency ($0 \leq \alpha < 1$), the EC50 of the drug increases as a result of the other drug (Figure 1C, quadrants II and III), corresponding to a decrease in potency (see Video S1 for an animated example of how the dose-response surface changes as a function of α). Since each drug can modulate the effective dose of the other independently (Zimmer et al., 2016), the 2D Hill equation contains two α values (α_1 and α_2) (Figure S1B, bottom and right edges of surface). This separation of α values in the 2D Hill equation makes it possible for a given drug combination to have synergism of potency in one direction ($\alpha_1 > 1$), and antagonism of potency in the other ($\alpha_2 < 1$), or vice versa (see Figure S1C for example surfaces).

Both MuSyC parameters for synergy of efficacy (β) and synergy of potency (α) correspond to geometric transformations of the dose-response surface, analogous to the parameters for efficacy (E_{max}) and potency (EC50) that transform the single-drug dose-response curve in classic pharmacology. We surveyed eight synergy methods to understand how they might account for these distinct types of synergy, including traditional methods of Bliss, Loewe, and highest single agent (HSA) (Gaddum, 1940), as well as more recent frameworks including the combination index (CI) (Chou, and Talalay, 1983), Zimmer et al.'s equivalent dose model (Zimmer et al., 2016), Schindler's PDE-Hill model (Schindler, 2017), ZIP (Yadav et al., 2015), and BRAID (Twarog et al., 2016). We find Bliss, Loewe, HSA, PDE-Hill, ZIP, and BRAID conflate synergy of efficacy and potency (Figures S2A–S2F) so that a drug combination with high synergistic potency scores identical to a combination with high synergistic efficacy (Figure S2A). This conflation, even in methods classically regarded as quantifying exclusively changes in efficacy, such as HSA, underscores the necessity of considering the entire

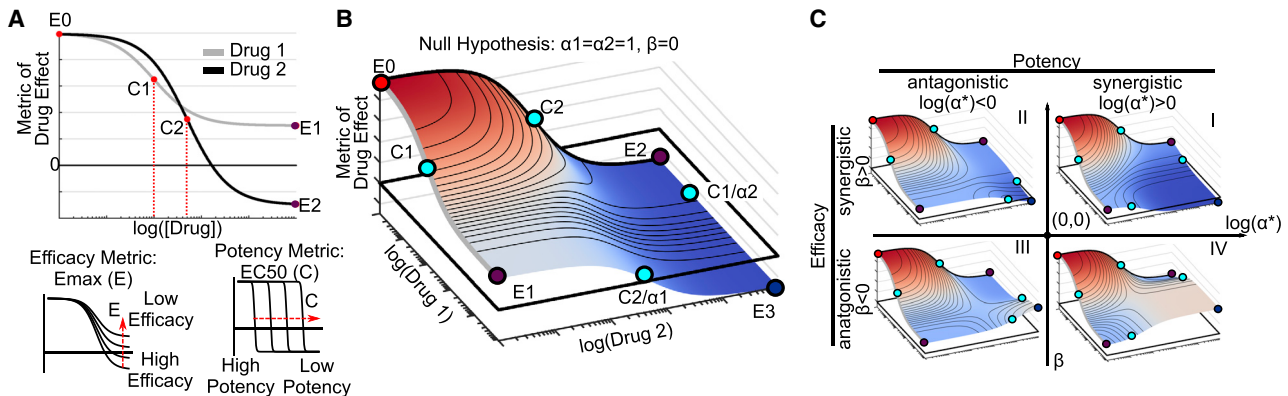


Figure 1. 2D Hill Equation Parameterizing Dose-Response Surfaces Distinguishes Synergistic Efficacy and Synergistic Potency

(A) Sigmoidal dose-response curves relating drug concentration to a measured effect are commonly fit to the Hill equation, derived from a 2-state model of drug effect (Figure S1A). The equation contains parameters for calculating a drug's potency, C , equal to the concentration required for half-maximal effect, and efficacy (E_{max}), equal to the maximal effect. Here, drug 1 is more potent than drug 2 ($C_1 < C_2$), while drug 2 is more efficacious ($E_2 < E_1$). For simplicity, in this diagram, we only depict a metric of drug effect for which increasing drug concentration results in lower values (e.g., anti-proliferative drugs). However, the same equation is valid for metrics that increase in value ($E_{max} > E_0$) (e.g., percent effect).

(B) A dose-response surface for drugs 1 and 2, based on the 2D Hill equation derived from a 4-state model of combination drug treatment (Figure S1B), under the null hypothesis of no synergy of efficacy ($\beta = 0$) or potency ($\alpha_1 = \alpha_2 = 1$).

(C) Representative dose-response surfaces for each quadrant on a drug synergy diagram (DSD). The vertical axis is divided into antagonistic ($\beta < 0$) and synergistic ($\beta > 0$) efficacy. The horizontal axis is divided into antagonistic ($\log(\alpha^*) < 0$) and synergistic ($\log(\alpha^*) > 0$) potency where α^* can be either α_1 or α_2 . Quadrant I corresponds to synergistic potency and efficacy. In contrast, combinations in quadrant IV have synergistic potency but antagonistic efficacy corresponding to a blunting in efficacy at lower doses. See Video S1, a depiction of the orthogonal effects of α and β on the dose-response surface.

topology of the dose-response surface in order to decouple synergistic efficacy from synergistic potency.

In other methods (equivalent dose and CI), only synergistic potency is tacitly assumed by asserting the maximal effect of each drug and of the combination is equal to zero (Figures S2G–S2J). (See STAR Methods, section Methods Details, subsection Comparison to alternative synergy models, for a case-by-case comparison of MuSyC with other synergy frameworks.)

By using the Hill equation as the basis for MuSyC, the metric of drug effect is not bounded to range between 0 and 1, as is the case for Bliss, CI, and the equivalent dose model, providing a greater versatility for application to other systems. Indeed, the challenges in applying prior synergy frameworks to our recently proposed metric of drug effect, the drug-induced proliferation (DIP) rate (Harris et al., 2016), provided the initial impetus for developing this framework.

In summary, the 2D Hill equation enables a formalism, termed MuSyC, in which synergistic efficacy and synergistic potency are orthogonal and quantified by the parameters β and α , respectively. We have provided an interactive MuSyC demo (see Data and Software Availability section in STAR Methods,) to facilitate an intuitive understanding of the relationship between different parameter values and the shape of the dose-response surface.

MuSyC Quantifies Synergy of Potency and Efficacy in a Drug Combination Screen

We applied MuSyC to evaluate the synergistic potency and efficacy of a 64-drug panel (see Table S2 for drugs, drug classes, nominal targets, and tested concentration ranges) in combination with osimertinib, a mutant EGFR-tyrosine kinase inhibitor recently approved for first-line treatment of EGFR-mutant NSCLC (Soria et al., 2018). The selected drugs span a diverse

array of cellular targets that can be broadly grouped into four categories: kinases, receptors and channels, epigenetic regulators, and mitotic checkpoints (Figure 2D), each with several sub-categories. The combinations were tested in PC9 cells, a canonical model of EGFR-mutant NSCLC (Jia et al., 2013) using a high-throughput, *in vitro*, drug-screening assay (Figure 2A). We quantified drug effect using the DIP rate metric (Harris et al., 2016), a metric that avoids temporal biases characteristic of traditional endpoint assays (see Quantification and Statistical Analysis section in STAR Methods, section).

To fit the resulting dose-response surfaces, we developed a Bayesian fitting algorithm, using a particle swarm optimizer (PSO) to seed priors for a Markov chain Monte Carlo (MCMC) optimization (Figures S3A and S3B; Quantification and Statistical Analysis section in STAR Methods). The algorithm also accounts for non-optimal drug dosage selection, since dose ranges that are insufficient to observe saturating effects—owing to limited solubility or potency of the drug—result in a commensurate increase in the uncertainty of MuSyC's synergy parameters (Figures S3C–S3E).

Applying this algorithm, we extracted synergy parameters (α_1 , α_2 , and β_{obs}) from fitted surfaces for all osimertinib combinations (β_{obs} is the observed synergistic efficacy at the maximum tested dose range) (see STAR Methods, section Methods Details).

The drug panel displays wide ranges of efficacy (E_2) and potency (C) for single agents (Figure S4A). The efficacy and potency of the single agents have no relationship with the synergistic efficacy and synergistic potency when combined with osimertinib (p value > 0.2) (Figure S4B), confirming MuSyC's synergy parameters are independent of single agents' dose-response curve and therefore, as expected, cannot be predicted from the single-agent, pharmacologic profiles.

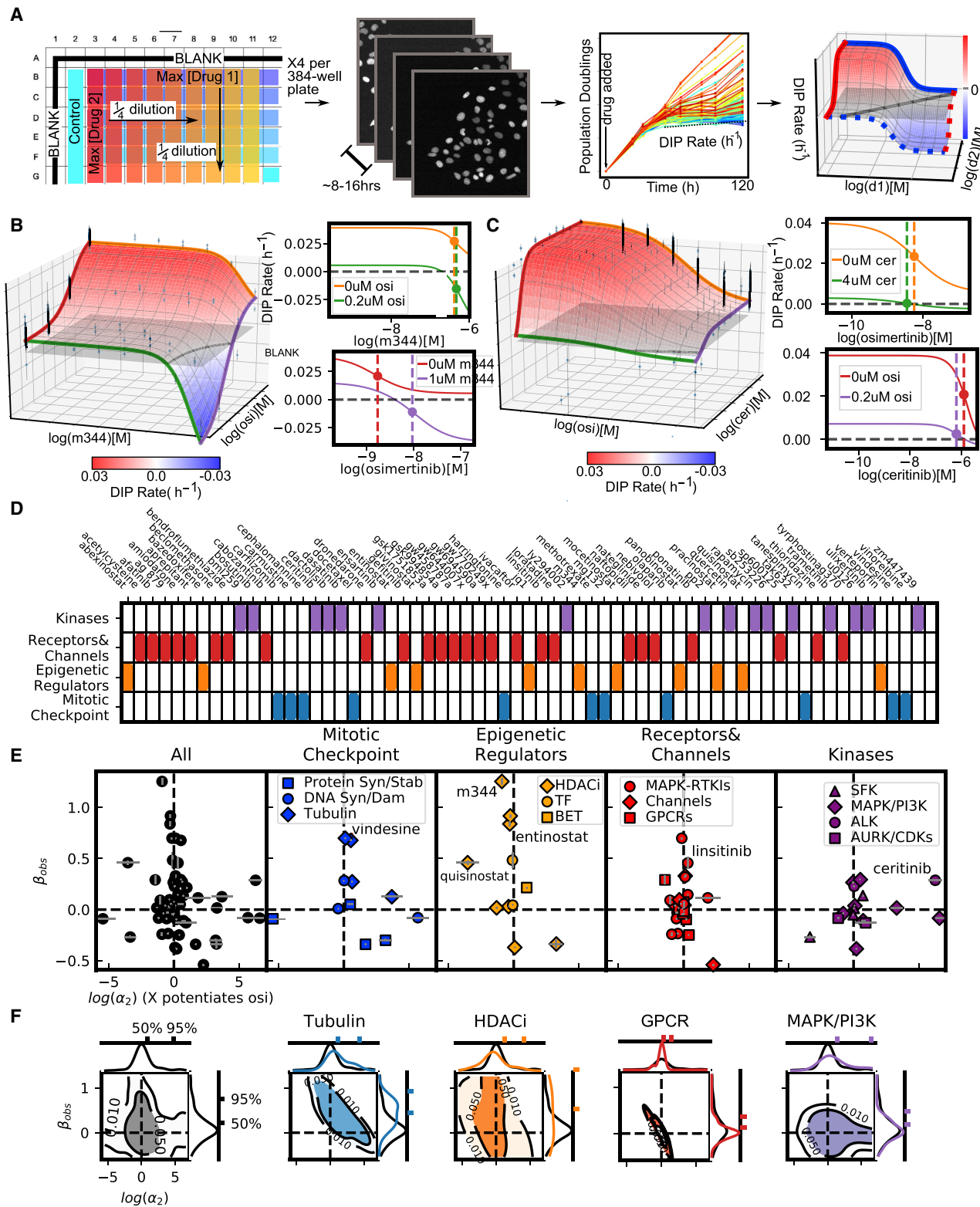


Figure 2. High-Throughput Screen of 64 Drugs Combined with Osimertinib (Mutant EGFR-TKI) Reveals Drug-Class Dependence of Synergistic Potency and Efficacy in NSCLC

(A) High-throughput pipeline for generating dose-response surfaces. Initial drug matrix is prepared on a 384-well plate and transferred to cells seeded at sub-confluent densities. Cells are engineered to express a fluorescently tagged histone (H2B-RFP), allowing for cell counts using automated segmentation software

(legend continued on next page)

Inspection of dose-response surfaces from this combination screen highlights the significance of resolving synergistic potency and efficacy. For instance, the dose-response surface for the osimertinib combination with M344 (a histone deacetylase [HDAC] inhibitor) exhibits synergistic efficacy ($\beta_{\text{obs}} = 1.25 \pm 0.03$, reflecting a 125% increase in efficacy over osimertinib alone) (Figures 2B and 2E). However, this improved efficacy comes at the cost of potency ($\log(\alpha_2) = -0.90 \pm 0.01$) as observed in the shift in the EC50 of osimertinib in the presence of 1 uM M344 (Figure 2B; red to purple dotted line). In contrast, ceritinib, an ALK inhibitor with off-target effects on IGF1R (Shaw et al., 2014), increases osimertinib's potency ($\log(\alpha_2) = 6.25 \pm 0.50$) (Figure 2C; green to orange dotted line) at 4 uM (maximal tested concentration) but with inconsequential improvement of efficacy ($\beta_{\text{obs}} = 0.28 \pm 0.003$).

To visualize synergy globally, we plotted drug combinations on DSDs, with observed synergistic efficacy (β_{obs}) and potency on the vertical and horizontal axes, respectively (Figure 2E). These DSDs reveal distinguishing trends between the four drug categories tested.

Within the mitotic checkpoint drugs, tubulin destabilizers (including vinodesine and vinorelbine) showed an upward shift along the axis of synergistic efficacy (Figure 2E). The marginal distribution confirmed this trend in comparison to all the drugs (Figure 2F, blue versus black vertical distributions). Similar results were obtained for the histone deacetylase inhibitor (HDACi) subgroup within the epigenetic regulators (Figures 2E and 2F). As expected, we observed limited synergistic or antagonistic efficacy for drugs targeting G-protein-coupled receptors (GPCRs) (Figures 2E and 2F; red versus black distributions). We also observed limited synergistic efficacy in directly co-targeting kinases in the MAPK pathway, suggesting this may be an unproductive avenue in EGFR-mutant NSCLC (Figures 2E and 2F; purple to black comparison along vertical axis).

In summary, by quantifying synergy of potency separate from synergy of efficacy, MuSyC reveals drug-class trends, which can be used to guide subsequent screens and drug combination deployment in NSCLC.

MuSyC Validates Co-targeting RAF and MEK in BRAF-Mutant Melanoma

The NSCLC drug screen (Figure 2) suggests combinations targeting molecules within the same signaling pathway may not be productive avenues for increasing efficacy. However, a com-

bination used clinically in BRAF-mutant melanoma co-targets kinases BRAF and MEK in the MAPK pathway (Long et al., 2014; Eroglu and Ribas, 2016). To investigate this combination in more detail, we screened a panel of 8 BRAFV600-mutant melanoma cell lines (see Paudel et al., 2018 for cell-line information) against 16 BRAFi/MEKi combinations (see Table S2 for drug information and tested dose ranges).

Based on the mean β_{obs} across cell lines, all 16 combinations were synergistically efficacious (Figures 3A and S5C), indicating MuSyC would have identified this treatment strategy prospectively. In contrast, conventional methods produce ambiguous results (Figure S6, top 3 panels in each cell line group), such that this combination strategy could have not been identified. Furthermore, MuSyC detected variations in synergistic efficacy between cell lines (Figures 3A and S5C), underscoring its sensitivity and pointing to heterogeneous, cell-intrinsic mechanisms modulating the efficacy of combined BRAF and MEK inhibition. In particular, A2058 displayed low average synergistic efficacy, suggesting that its canonical insensitivity to BRAFi does not depend on MEK reactivation but rather on altered metabolic phenotype (Parmenter et al., 2014; Hardeman et al., 2017).

MuSyC also provides information on synergistic potency for these combinations. A clinically deployed combination (dabrafenib and trametinib) is synergistically efficacious but antagonistically potent in all cell lines except one (Figure S5), a trade-off that may be relevant in the clinic.

Together, MuSyC analyses of NSCLC and of melanoma combination screens indicate that the magnitude of a drug combination's synergistic efficacy depend upon the oncogenetic context, i.e., co-targeting within the MAPK pathway may work for mutant-BRAF melanoma but not for mutant-EGFR NSCLC.

MuSyC Reveals Whether Molecular Correlates of Insensitivity Alter Synergistic Efficacy or Potency

While drug combinations are commonly identified from top-down approaches, e.g., high-throughput drug screens, others, including BRAFi/MEKi, were discovered from a bottom-up approach by investigating molecular correlates of insensitivity. However, these molecular correlates may alter either the potency or the efficacy of the primary drug (or both). MuSyC can distinguish among these possibilities, enabling an informed choice between improving either efficacy or potency. As an example, we looked for molecular correlates of BRAFi insensitivity between subclones of a BRAF-mutant melanoma cell line

(see STAR Methods section Quantification and Statistical Analysis). Each condition is imaged every 6–8 h, resulting in growth curves. The growth curves are fit for the DIP rate (slope of dotted line) (Harris et al., 2016) to quantify drug effect. This matrix of DIP rates is fit to the 2D Hill equation to extract synergy parameters. (B) Combination surface of M344, an HDACi, and osimertinib (osi). Gray plane indicates a cytostatic growth rate (i.e., DIP rate = 0 h⁻¹). Left are the dose-response curves for each drug alone (orange and red curves) and each drug with the maximum tested concentration of the other (green and purple). Colors correspond to the colored lines on the combination surface. The dotted lines demarcate the EC50 for each curve. (C) Combination surface for ceritinib (cer), an ALK, in combination with osimertinib. Ceritinib increases the potency of osimertinib at maximum tested concentration, as observed in the shift of the EC50 between orange and green curves in the top left panel. The shift is proportional to the concentration used and would, therefore, increase at higher concentrations; however, such concentrations are not physiologically realizable because of the low potency of ceritinib in this system (EC50 = 2.02 uM), highlighting the importance of interpreting synergistic potency in the context of the absolute potency. (D) Drug panel used in combination with osimertinib grouped in 4 categories (see Table S2 for details). (E) DSDs for drug combinations. The vertical axis quantifies the observed synergistic efficacy (β_{obs}). The horizontal axis ($\log(\alpha_2)$) quantifies how osimertinib's potency is modulated by each drug (see Figure S4C for α_1 - α_2 plot). Error bars represent the parameter uncertainty based on the MCMC optimization (see STAR Methods for description of fitting algorithm). (F) 2D density plots and associated marginal distributions for β_{obs} (vertical axis) and α_2 (horizontal axis) for all drugs (black) and selected category subclasses. Colored tick marks indicate the 50% and 95% probability density intervals for each distribution.

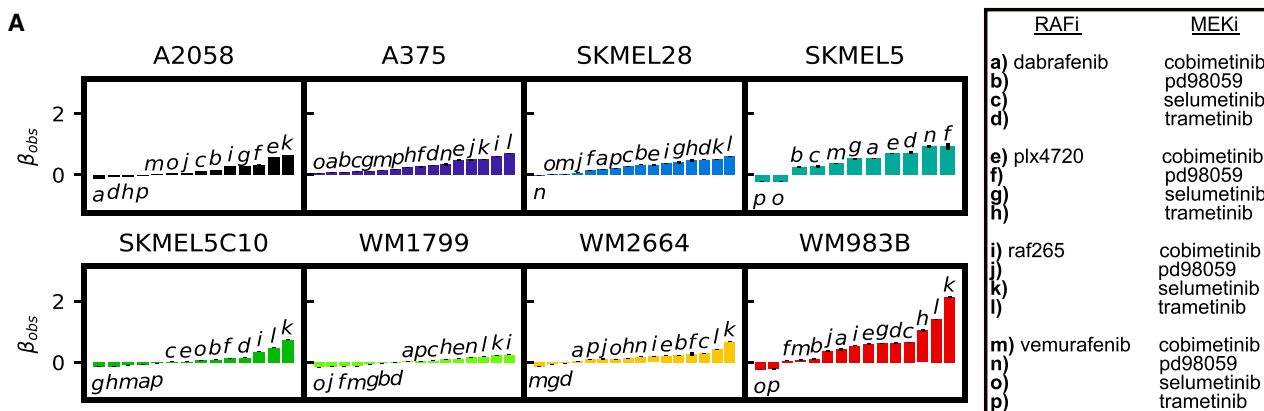


Figure 3. Synergistic Efficacy and/or Potency of Drug Combinations in BRAF-Mutant Melanoma

(A) 8 BRAF-mutant melanoma cell lines were treated with all possible pairwise combinations of 4 RAF and 4 MEK inhibitors (Table S2) for a total of 128 unique combinations. Waterfall plots of $\beta_{0\text{obs}}$ for each cell line with all combinations, which converged in fitting. Drug combinations noted by letter in the legend to right. (also see Figure S5).

(SKMEL5) with differential sensitivity to BRAFi (Figure 4A). Specifically, we quantified gene expression using RNA sequencing (RNA-seq) and identified the top 200 differentially expressed genes (DEGs) ($\text{FDR} < 0.001$; see STAR Methods section Quantification and Statistical Analysis). This gene set was significantly enriched in processes, cellular components, and molecular functions relating to metabolism (Figure 4B), aligning with previous reports on the relationship between altered metabolism and resistance to BRAFi (Parmenter et al., 2014; Hardeman et al., 2017). We computed the correlation of the 200 DEGs' expression to BRAFi sensitivity across a 10-cell-line panel (see STAR Methods) using expression data from Subramanian et al. (2017). NOX5 stood out as one of five genes with a significant, positive correlation with BRAFi insensitivity (Pearson $r = 0.65$; p value = 0.042) (Figures 4C and 4D; Table S3 for quantification of BRAFi insensitivity and Table S4 for genes correlated with BRAFi insensitivity) and was significantly up-regulated in the BRAFi-insensitive subclone (SC10) compared with the sensitive subclone (SC01) (Figure 4E). Previously unconsidered, NOX5 is an interesting target because of its convergent regulation on metabolic and redox signaling at mitochondria (Lu et al., 2012), processes significantly enriched in the DEGs (Figure 4B).

To study NOX5's contribution to the potency or efficacy of BRAFi, we tested PLX4720 in combination with a NOX5 inhibitor, DPI (Jaquet et al., 2011), in a panel of 7 melanoma cell lines selected based on differential NOX5 expression. We found synergistic efficacy correlated with NOX5 expression (Pearson $r = 0.77$; p value = 0.043) (Figures 4G and 4H); however, synergistic potency did not (Pearson $r = 0.01$; p value = 0.96) (Figures 4G and 4I). Of note, A2058, well known for its resistance to BRAFi, exhibited the highest NOX5 expression among the cell lines and the highest synergistic efficacy ($\beta_{0\text{obs}} = 1.42 \pm 0.05$) (Figure 4F), which was more synergistically efficacious than all tested MEKi/BRAFi combinations (Figure 3A).

Taken together, these results suggest co-targeting NOX5 in BRAF-mutant melanoma could lead to improved outcomes for BRAF-mutant melanoma patients with a unique metabolic program for which NOX5 is a biomarker. Furthermore, this study

demonstrates the utility of MuSyC for distinguishing a molecular constituent's role in modulating the potency or efficacy of a drug.

MuSyC Generalizes Traditional Synergy Metrics and Removes Biases and Ambiguities

To investigate how results from MuSyC compare with the most frequently used synergy metrics, we calculated synergy using Loewe additivity, CI, and Bliss on data from the NSCLC (Figure 2) and the melanoma (Figure 3A) screens. Loewe synergy was calculated directly from the DIP rate data, while CI and Bliss, which require percent metrics, were calculated from 72-h percent viability (Barretina et al., 2012) imputed from the growth curves (see STAR Methods section Quantification and Statistical Analysis). Unlike MuSyC, these metrics are evaluated at every concentration, resulting in dose-dependent distributions of synergy (Figures 5A and S6) commonly resulting in an ambiguous classification of a combination. By the median of each distribution, none of the metrics can statistically discriminate between the MuSyC DSD quadrants (Figures 5A and S6; Kruskal-Wallis p value > 0.05).

Examining the models underlying these metrics revealed several limitations and biases accounting for their ambiguity. For Loewe additivity, synergy is undefinable for many tested concentrations as Loewe cannot be calculated at combination conditions with effects exceeding the maximum effect of the weaker drug (Fouquerier and Guedj, 2015). This is particularly limiting for synergistically efficacious combinations, which, by definition, achieve greater effect than either drug alone. In the NSCLC screen, because osimertinib alone was not sufficient to achieve a negative DIP rate (i.e., regressing population), Loewe is undefinable for all conditions where the DIP rate was less than zero (Figure 5B). For conditions where Loewe is defined, Loewe additivity has been reported to be most appropriate for combinations of mutually exclusive inhibitors (Chou and Talalay, 1984). Accordingly, we found Loewe emerges from MuSyC as a special case under the conditions of both $\alpha_1 = \alpha_2 = 0$ (i.e., the drugs are mutually exclusive) and $h_1 = h_2 = 1$ (see STAR Methods, section Methods Details, subsection 2.1). If the

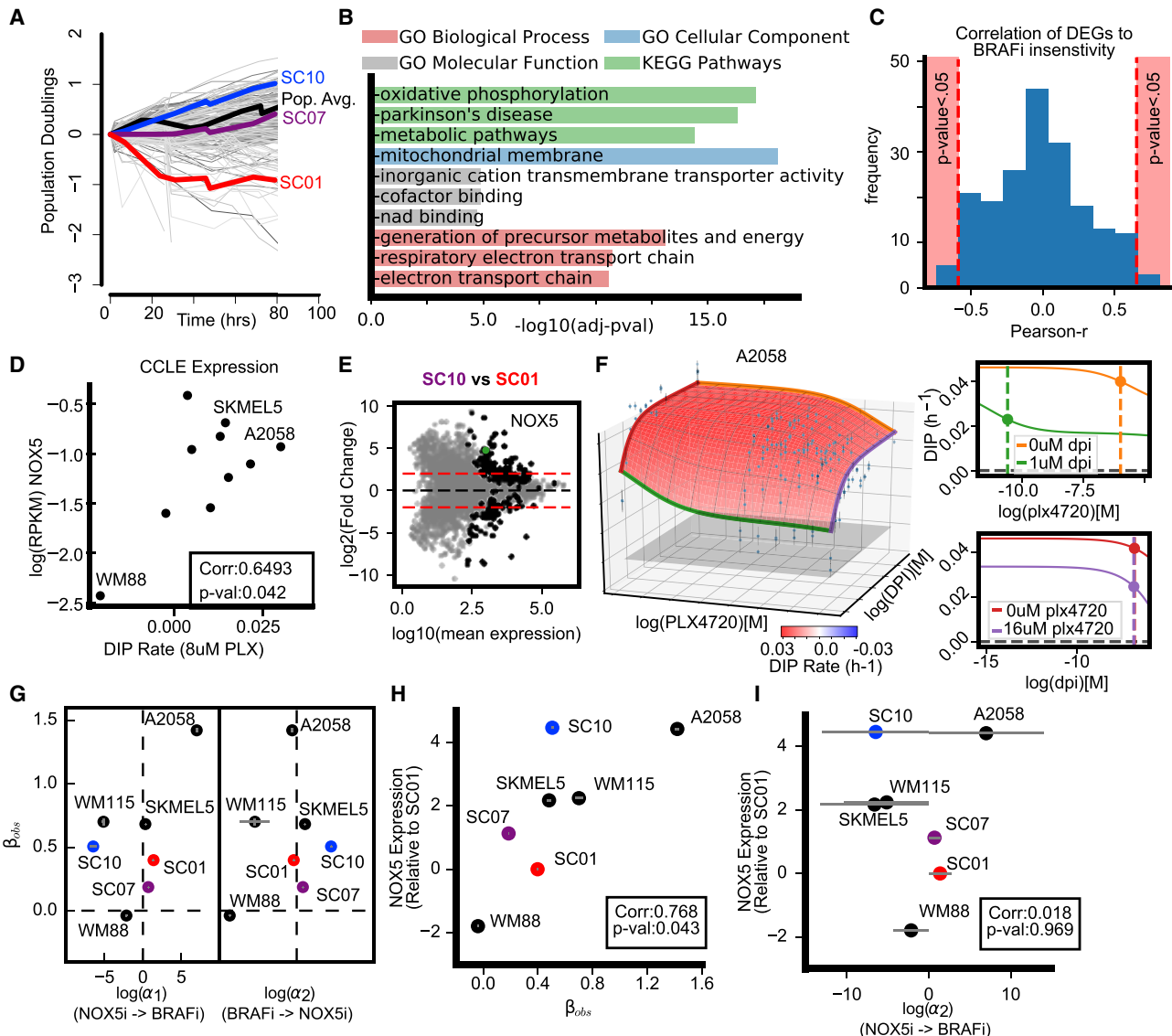
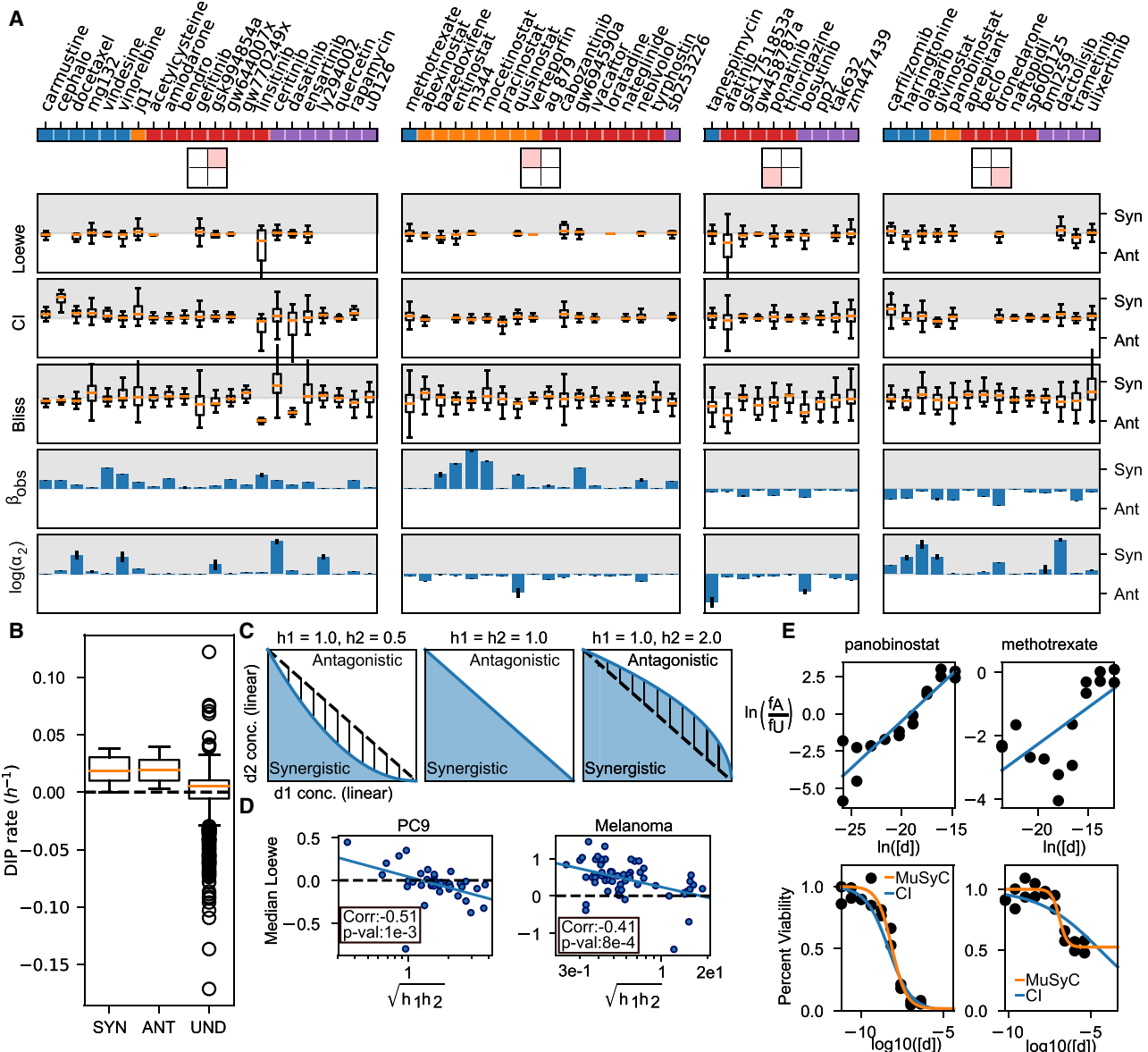


Figure 4. NOX5, a Molecular Correlate of Insensitivity to BRAFi, Is a Synergistically Efficacious Co-target in BRAF-Mutant Melanoma

- (A) Growth curves of differentially sensitive, single-cell-derived subclones from SKMEL5 treated with 8 uM PLX4720. Gray curves represent colony growth according to the clonal fractional proliferation assay (Tyson et al., 2012). The average population response indicated in black curve. SC01, SC07, and SC10 were subsequently used to identify 200 DEGs.
- (B) Top gene set enrichment terms for 200 DEGs (see STAR Methods section Quantification and Statistical Analysis).
- (C) Distribution of the correlation between 200 DEGs' expression and BRAFi insensitivity. Drug sensitivity was quantified as DIP rate measured in 8 uM PLX4720 (Table S3). Significance threshold of p value < 0.05 annotated in pink.
- (D) NOX5 expression correlates with BRAFi sensitivity in 10 BRAF-mutant melanoma cells.
- (E) Pairwise comparison between SC01 and SC10 of DEGs (FDR < 0.001) identified using DESeq2 (Love et al., 2014). The 200 identified DEGs (ANOVA between three subclones) are in black. Dotted red lines denote ± 4 -fold change.
- (F) Dose-response surface for PLX4720+DPI (NOX5 inhibitor) in A2058.
- (G) DSD for NOX5i (DPI) plus BRAFi (PLX4720). Error bars represent parameter uncertainty calculated in MCMC fitting.
- (H) Correlation (Pearson r) of NOX5 expression with observed synergistic efficacy (β_{obs}).
- (I) Correlation (Pearson r) of NOX5 expression with synergistic potency (α_2 = DPI's effect on PLX4720 potency).

condition $h_1 = h_2 = 1$ is not satisfied (Figure 5C), MuSyC predicts that when the geometric mean of the hill slopes is less than 1 ($\sqrt{h_1 * h_2} < 1$), the linear model of Loewe will overestimate synergy and when $\sqrt{h_1 * h_2} > 1$, Loewe will underestimate synergy (Figure 5C). Correspondingly, we found the median value of

Loewe synergy was negatively correlated with the geometric mean of the hill coefficients in both the NSCLC and melanoma screens (Figure 5D, Spearman $r = -0.51$ and -0.41 ; p value = $1e-3$ and $8e-4$, respectively); that is, the synergy of a combination according to Loewe additivity could be estimated based on

**Figure 5. Biases and Limitations of Loewe, CI, and Bliss**

(A) Drugs are separated based on their DSD quadrant from Figure 2, and distributions of synergy calculated by Loewe, CI, and Bliss are shown. Loewe was calculated directly from DIP rates, while CI and Bliss were calculated from 72-h viability (see STAR Methods section Methods Details). Overall, most combinations span synergism and antagonism when quantified by Loewe, CI, or Bliss. Conditions for which synergy could not be defined were removed. Traditionally, Loewe and CI are synergistic between 0 and 1 and antagonistic for values > 1; however, for visualization, we transformed them to $-\log(\text{Loewe})$ and $-\log(\text{CI})$, so synergism (Syn) corresponds to positive numbers (gray region) and antagonism (Ant) to negative (white region). α_2 is the change in osimertinib's potency because of the other drug. Error bars for β_{obs} and $\log(\alpha_2)$ calculated from MCMC optimization.

(B) Loewe is undefined (Und) for all concentrations, which achieved a net negative DIP rate.

(C) Loewe and CI assume the dose-response surface contours (i.e., the DIP rate axis comes out of the page) are linear (middle panel). The blue and white areas indicate regions that are synergistic and antagonistic, respectively, by MuSyC. When $\sqrt{h_1 * h_2} < 1$ (left panel), Loewe and CI misclassify the hatched region as synergistic, while when $\sqrt{h_1 * h_2} > 1$ (right panel), they misclassify the hatched region as antagonistic.

(D) As predicted, the median values of synergy calculated by Loewe are anti-correlated with the geometric mean of the hill slope in both the NSCLC and BRAF-mutant melanoma datasets.

(E) CI poorly fits drugs whose max effect is not equal to 0. The top panel shows linear dose-response fit by the CI algorithm; bottom shows the quality of fit in a standard dose-response view. The CI fit works well for drugs for which $E_{\text{max}} \approx 0$, such as panobinostat (left, $E_{\text{max}} = 0.016$, $C = 7.13$ nM, $h_2 = 0.99$ for orange fit, $E_{\text{max}} = 0$, $C = 4.42$ nM, $h_2 = 0.63$ by CI). However, drugs with $E_{\text{max}} >> 0$, such as methotrexate (right) lead to poor fits ($E_{\text{max}} = 0.52$, $C = 0.119$ uM, $h_2 = 1.88$ by orange fit, $E_{\text{max}} = 0$, $C = 34.7$ uM, $h_2 = 0.23$ by CI).

the hill slope of a single drug alone in contrast to MuSyC where synergistic potency and efficacy are decoupled from the single drug's pharmacologic profile (Figure S3B).

CI is a special case of Loewe additivity that adds the additional condition that $E_0 = 1$, $E_1 = E_2 = E_3 = 0$, such that the drug effect is equated with percent inhibition (Chou and Talalay, 1983). The condition on effect range assumes all drugs achieve the same maximum effect, and thus, unlike Loewe additivity, CI range is not limited by the weaker drug. However, in percent viability data, many drugs do not achieve 0% viability (e.g., methotrexate, which reaches a maximum effect of 52% viability) (Figure 5E). In these cases, fits for the single-drug dose-response curves used to calculate CI are poor (Figure 5E). CI is thus inappropriate for cell-based assays of drug effect where the correspondence between percent inhibition and cell viability is not one-to-one.

Bliss, similar to CI, can only be applied to percent metrics with the condition $E_0 = 1$, $E_1 = E_2 = E_3 = 0$. As with CI, because most drugs in combination do not satisfy this condition, Bliss is also an inappropriate model to use. However, if this condition is satisfied, Bliss emerges as a special case of MuSyC under the conditions $\alpha_1 = \alpha_2 = 1$ (see STAR Methods section Methods Details, subsection 2.2).

In summary, MuSyC subsumes Loewe (and therefore CI) and Bliss into a single framework satisfying both the dose additivity and the multiplicative survival principles under certain conditions. For combinations that do not satisfy these conditions, we show the traditional metrics lead to biased and ambiguous results, while MuSyC's generality resolves these limitations. Specifically these limitations are as follows: traditional methods cannot distinguish synergy of potency from synergy of efficacy (Figures 5A and S2); Loewe is undefined for combinations with synergistic efficacy (Figure 5B); Loewe (and by extension CI) contain an artificial bias toward synergy for drugs with hill slopes much less than 1 (Figures 5C and 5D); and CI leads to poor fits because it disregards synergistic efficacy by assuming that the maximal effect of a drug reaches 0%, even when this is not the case (Figure 5E).

DISCUSSION

The goal of using synergistic drugs is to achieve more with less. It is therefore intuitive that two types of synergy exist: one corresponding to how much more is achievable (synergistic efficacy) and the other to how much less is required (synergistic potency). Finding such combinations is vital for optimizing therapeutic windows, as there exists a fundamental trade-off between clinical efficacy and tolerable doses. Diseases for which single-drug efficacy is sufficient would benefit from synergistically potent combinations to drive down toxicity and/or side effects. Diseases with treatments of insufficient efficacy are in pressing need of synergistically efficacious combinations in order to improve the depth and durability of response. By stratifying synergy along distinct axes of potency and efficacy using MuSyC, informed choices can be made about this trade-off. The distinction facilitates identifying drug-class trends that can be iteratively expanded in future screens to optimize synergistic efficacy or synergistic potency, whichever is desirable for a particular disease.

In this respect, MuSyC provides a global view of the synergistic behavior of whole classes of drugs, e.g., from a high-throughput drug screen, via DSDs. In this work, MuSyC revealed a subclass of epigenetic regulators as potentially interesting targets for combination therapy in an EGFR-oncogene-addicted background. Epigenetic regulators have previously been suggested to prime NSCLC for sensitivity to EGFRi (Schiffmann et al., 2016), and the HDACi entinostat in combination with erlotinib (first generation EGFR-TKI) has been shown to increase overall survival in EGFR-mutant NSCLC cases with high expression of E-cadherin (Witta et al., 2006, 2012). Consistent with this, we also observe entinostat was synergistically efficacious with osimertinib ($\beta_{obs} = 0.84 \pm 0.027$) in PC9 cells, an E-cadherin high-expressing cell line (Shimoyama et al., 1992). As is typical of high-throughput screens, there were results of undetermined significance, including dronedarone (an anti-arrhythmic sodium channel inhibitor) and GW694590a (an anti-angiogenesis compound targeting the TIE2 receptor), which were the most antagonistic and synergistically efficacious compounds out of the receptors and channels drug classes, respectively. Further studies are needed to verify these results. Nonetheless, MuSyC provides a quantitative foundation to further investigate unsuspected combinations.

The global views provided by the MuSyC DSDs also reveal synergistic trends that vary according to disease context. For example, co-targeting the MAPK pathway in NSCLC or BRAF-mutant melanoma yields different outcomes: in the former, only synergistic potency is observed, while in the latter, synergistic efficacy, and sometimes potency, are registered. The disparity emphasizes that synergistic trends require data-driven metrics that distinguish between synergy of efficacy and potency.

MuSyC dose-response surfaces facilitate evaluating the significance that combination synergy should be assigned; that is, MuSyC's synergy parameters quantify the *relative* increase in efficacy or potency of the combination, with respect to single agents, and therefore, the improvements should be interpreted in the context of the absolute potency and efficacy. This information is directly conveyed in the topology of the dose-response surface. As an example, in the NSCLC screen, the combination of osimertinib with quisinostat exhibited the greatest total efficacy. However, since quisinostat is already significantly efficacious on its own, that combination ranks lower than the M344-osimertinib combination along the axis of synergistic efficacy on a DSD. Thus, DSDs are useful to rank relative increase in potency or efficacy, whereas surfaces convey the absolute efficacy and potency achieved by a combination.

MuSyC is also useful for investigating a molecular species' contribution to the potency and efficacy of a compound. Here, we demonstrated NOX5 activity modulates the efficacy but not the potency, of BRAFi. However, the NOX5i used, DPI, is known to have off-target effects (Altenhöfer et al., 2015); therefore, further evidence for the role of NOX5 in BRAFi efficacy will require extending MuSyC to studies combining drugs and gene silencing technology (e.g., RNAi or CRISPR).

To fit the dose response surface and extract synergy parameters, MuSyC utilizes a Bayesian approach combining PSO and a multi-tier MCMC walk in order to track uncertainty in the values for synergistic potency and efficacy. The sources for this

uncertainty include noise, partial dose-response curves, and data density. A similar Bayesian approach was previously implemented for Loewe (Hennessey et al., 2010).

Loewe additivity and Bliss independence have maintained dominance in the field, along with the related work of Chou and Talalay. Yet there is no consensus regarding the appropriate use of these methods because they are based on distinct foundational principles, often leading to incompatible results (Greco et al., 1992). MuSyC removes these sources of confusion by unifying these methods into a consensus framework, within which Loewe and Bliss emerge as special cases.

There has been much critical analysis over the past 25 years on the term “synergy” (Greco et al., 1992), arguably rooted in the practice of defining synergy with respect to arbitrary expectations of drug additivity implicitly codified in previous methods’ foundational principles. In contrast, ambiguity about the meaning of synergy disappears in MuSyC because its synergy parameters relate directly to the textbook pharmacology concepts of efficacy and potency. Indeed, a major advance of MuSyC is the decisive shift toward synergy calculations directly related to an observable change in efficacy and/or potency. Thus, ambiguous questions such as “Is there synergy?” can be recast into more precise questions, such as “How much does efficacy or potency of drug X change when drug Y is added?” Such precise language should promote a move away from arbitrary cutoffs for “significant synergy,” which are context dependent.

While we focused on the DIP rate as our metric of effect, MuSyC may be applied to any quantifiable phenotype whose dose response is suitable to be fit by a Hill equation. In contrast, all other synergy models we surveyed impose strict constraints on the type and/or magnitude of the drug effect metric. Thus, MuSyC opens up the potential to study synergy of drug effects previously impossible to address by existing methods. Examples of metrics include immune activation, growth in 3D culture, or second messenger efflux. The flexibility is particularly critical in translating drug combinations to the clinic by using models of increasing complexity, such as organoids, which better represent the drug sensitivity of a patient (Jabs et al., 2017). Indeed, that most clinical combinations can be explained by patient-to-patient variability (Palmer and Sorger, 2017) is a strong rationale for translating combination screens to more complex, pre-clinical models. Subsequent work will be devoted to scaling the combination drug screening pipeline developed here to pre-clinical experimental models of increasing complexity, such as organoids.

In conclusion, we have presented MuSyC, a drug synergy framework that maintains a distinction between two intuitive types of pharmacological synergy and that may be applied to any drug effect metric. We showed this framework allows for a richer understanding of drug interactions, with practical, translational consequences. We foresee this approach will streamline drug discovery pipelines and facilitate the deployment of precision approaches to therapeutic combinations.

STAR★METHODS

Detailed methods are provided in the online version of this paper and include the following:

- KEY RESOURCES TABLE
- CONTACT FOR REAGENT AND RESOURCE SHARING
- EXPERIMENTAL MODEL AND SUBJECT DETAILS
- METHODS DETAILS
 - Key Equations
 - Comparison to Alternative Synergy Models
 - Sham Experiment
 - Derivation of Generalized 2-Dimensional Hill Equation
 - Four-state model with multiple steps between states
 - Combination Experiments Protocol
 - RNA-seq of Melanoma Cell Lines
 - RT-qPCR Quantification of NOX5 Expression
- QUANTIFICATION AND STATISTICAL ANALYSIS
 - Fitting Dose-Response Surfaces
 - Calculating the DIP Rate
 - Calculating Loewe, CI, Bliss, and HSA
 - Fitting ZIP, BRAID, Schindler’s Hill PDE, and Equivalent Dose Models
 - Identifying DEGs for GO Enrichment Analysis
- DATA AND SOFTWARE AVAILABILITY

SUPPLEMENTAL INFORMATION

Supplemental Information can be found with this article online at <https://doi.org/10.1016/j.cels.2019.01.003>.

ACKNOWLEDGMENTS

The authors would like to thank Corey Hayford, Sarah Maddox, Carlos Lopez, and Chris Wright for insightful conversations; Jing Hao for the help with experimental preparation and reagent procurement; and James Pino and Alexander Lubbock for the pythonic implementation of PSO and findDIP libraries, respectively.

Experiments were performed in the Vanderbilt HTS Core Facility, an institutionally supported core with assistance provided by Debbie Mi, Page Vinson, and Joshua Bower.

This work was supported by the following funding sources: C.T.M. was supported by the National Science Foundation (NSF) Graduate Student Fellowship Program (GRFP) [Award #1445197]. V.Q. was supported by the National Institutes of Health (NIH) (U54-CA217450, R01-186193, and U01-CA215845); J.B. was supported by the National Cancer Institute (NCI) (R50-CA211206). D.W. was supported by Ruth L. Kirschstein National Research Service Award (2T32HL094296-06A1). C.M.L. was supported in part by the NIH (P30-CA086485, R01-CA121210, and P01-CA129243). C.M.L. additionally was supported by a V Foundation Scholar-in-Training Award, an AACR-Genentech Career Development Award, a Damon Runyon Clinical Investigator Award, a LUNGevity Career Development Award, and a Lung Cancer Foundation of America/International Association for the Study of Lung Cancer Lori Monroe Scholarship.

AUTHOR CONTRIBUTIONS

Conceptualization, C.T.M., D.J.W., L.A.H., D.R.T., and V.Q.; Methodology, C.T.M., D.R.T., and J.B.; Software, C.T.M. and D.J.W.; Investigation, C.T.M., D.W., B.B.P., K.N.H., D.R.T., L.A.H., and J.B.; Formal Analysis, C.T.M., D.J.W., B.B.P., and D.R.T.; Resources, D.R.T., J.B., and D.W.; Data Curation, C.T.M. and D.R.T.; Writing – Original Draft, C.T.M., D.J.W., L.A.H., and V.Q.; Writing – Review & Editing, C.T.M., D.J.W., B.B.P., D.R.T., C.M.L., D.W., J.B., L.A.H., and V.Q.; Visualization, C.T.M., D.J.W., and B.B.P.; Supervision, L.A.H., D.R.T., and V.Q.; Funding Acquisition, D.R.T. and V.Q.

DECLARATION OF INTERESTS

The authors declare no competing interests.

Received: May 17, 2018
 Revised: August 22, 2018
 Accepted: January 14, 2019
 Published: February 20, 2019

REFERENCES

- Altenhöfer, S., Radermacher, K.A., Kleikers, P.W., Wingler, K., and Schmidt, H.H. (2015). Evolution of NADPH oxidase inhibitors: selectivity and mechanisms for target engagement. *Antioxid. Redox Signal.* **23**, 406–427.
- Ashton, J.C. (2015). Drug combination studies and their synergy quantification using the Chou–Talalay method—letter. *Cancer Res.* **75**, 2400.
- Barretina, J., Caponigro, G., Stransky, N., Venkatesan, K., Margolin, A.A., Kim, S., Wilson, C.J., Lehár, J., Kryukov, G.V., Sonkin, D., et al. (2012). The Cancer Cell Line Encyclopedia enables predictive modelling of anticancer drug sensitivity. *Nature* **483**, 603–607.
- Berg, A., Meyer, R., and Yu, J. (2004). Deviance information criterion for comparing stochastic volatility models. *J. Bus. Econ. Stat.* **22**, 107–120.
- Bliss, C.I. (1939). The toxicity of poisons applied jointly. *Ann. Appl. Biol.* **26**, 585–615.
- Chou, T.C. (2010). Drug combination studies and their synergy quantification using the Chou–Talalay method. *Cancer Res.* **70**, 440–446.
- Chou, T.-C., and Talalay, P. (1983). Analysis of combined drug effects: a new look at a very old problem. *Trends Pharmacol. Sci.* **4**, 450–454.
- Chou, T.C., and Talalay, P. (1984). Quantitative analysis of dose-effect relationships: the combined effects of multiple drugs or enzyme inhibitors. *Adv. Enzyme Regul.* **22**, 27–55.
- Eroglu, Z., and Ribas, A. (2016). Combination therapy with BRAF and MEK inhibitors for melanoma: latest evidence and place in therapy. *Ther. Adv. Med. Oncol.* **8**, 48–56.
- Fallahi-Sichani, M., Honarnejad, S., Heiser, L.M., Gray, J.W., and Sorger, P.K. (2013). Metrics other than potency reveal systematic variation in responses to cancer drugs. *Nat. Chem. Biol.* **9**, 708–714.
- Foucquier, J., and Guedj, M. (2015). Analysis of drug combinations: current methodological landscape. *Pharmacol. Res. Perspect.* **3**, e00149.
- Gaddum, J.H. (1940). *Pharmacology* (Oxford University Press).
- Gong, Z., Hu, G., Li, Q., Liu, Z., Wang, F., Zhang, X., Xiong, J., Li, P., Xu, Y., Ma, R., et al. (2017). Compound libraries: recent advances and their applications in drug discovery. *Curr. Drug Discov. Technol.* **14**, 216–228.
- Greco, W., Unkelbach, H.-D., Pöch, G., Sühnel, J., Kundi, M., and Bödeker, W. (1992). Consensus on concepts and terminology for combined-action assessment: the Saariselsa Agreement. *Arch. Complex Environ. Stud.* **4**, 65–69.
- Greco, W.R., Bravo, G., and Parsons, J.C. (1995). The search for synergy: a critical review from a response surface perspective. *Pharmacol. Rev.* **47**, 331–385.
- Hafner, M., Niepel, M., Chung, M., and Sorger, P.K. (2016). Growth rate inhibition metrics correct for confounders in measuring sensitivity to cancer drugs. *Nat. Methods* **13**, 521–527.
- Hardeman, K.N., Peng, C., Paudel, B.B., Meyer, C.T., Luong, T., Tyson, D.R., Young, J.D., Quaranta, V., and Fessel, J.P. (2017). Dependence on glycolysis sensitizes BRAF-mutated melanomas for increased response to targeted BRAF inhibition. *Sci. Rep.* **7**, 42604.
- Harris, L.A., Frick, P.L., Garbett, S.P., Hardeman, K.N., Paudel, B.B., Lopez, C.F., Quaranta, V., and Tyson, D.R. (2016). An unbiased metric of antiproliferative drug effect in vitro. *Nat. Methods* **13**, 497–500.
- He, B., Lu, C., Zheng, G., He, X., Wang, M., Chen, G., Zhang, G., and Lu, A. (2016). Combination therapeutics in complex diseases. *J. Cell. Mol. Med.* **20**, 2231–2240.
- Hennessey, V.G., Rosner, G.L., Bast, R.C., Jr., and Chen, M. (2010). A Bayesian approach to dose-response assessment and synergy and its application to in vitro dose-response studies. *Biometrics* **66**, 1275–1283.
- Hunter, J.D. (2007). Matplotlib: a 2D graphics environment. *Comput. Sci. Eng.* **9**, 90–95.
- Jabs, J., Zickgraf, F.M., Park, J., Wagner, S., Jiang, X., Jechow, K., Kleinheinz, K., Toprak, U.H., Schneider, M.A., Meister, M., et al. (2017). Screening drug effects in patient-derived cancer cells links organoid responses to genome alterations. *Mol. Syst. Biol.* **13**, 955.
- Jaquet, V., Marcoux, J., Forest, E., Leidal, K.G., McCormick, S., Westermaier, Y., Perozzo, R., Plastre, O., Fioraso-Cartier, L., Diebold, B., et al. (2011). NADPH oxidase (NOX) isoforms are inhibited by celastrol with a dual mode of action. *Br. J. Pharmacol.* **164**, 507–520.
- Jia, P., Jin, H., Meador, C.B., Xia, J., Ohashi, K., Liu, L., Pirazzoli, V., Dahlman, K.B., Politi, K., Michor, F., et al. (2013). Next-generation sequencing of paired tyrosine kinase inhibitor-sensitive and -resistant EGFR mutant lung cancer cell lines identifies spectrum of DNA changes associated with drug resistance. *Genome Res.* **23**, 1434–1445.
- Jones, E., Oliphant, T., and Peterson, P. (2001). SciPy: open source scientific tools for python. <http://www.scipy.org>.
- Kim, D., Langmead, B., and Salzberg, S.L. (2015). HISAT: a fast spliced aligner with low memory requirements. *Nat. Methods* **12**, 357–360.
- Kuleshov, M.V., Jones, M.R., Rouillard, A.D., Fernandez, N.F., Duan, Q., Wang, Z., Koplev, S., Jenkins, S.L., Jagodnik, K.M., Lachmann, A., et al. (2016). Enrichr: a comprehensive gene set enrichment analysis web server 2016 update. *Nucleic Acids Res.* **44**, W90–W97.
- Lebigot, E.O. (2011). Uncertainties: a Python package for calculations with uncertainties. <https://pypi.org/project/uncertainties/>.
- Liao, Y., Smyth, G.K., and Shi, W. (2014). featureCounts: an efficient general purpose program for assigning sequence reads to genomic features. *Bioinformatics* **30**, 923–930.
- Loewe, S., and Muischnek, H. (1926). über Kombination swirkungen. *Archiv. Experiment. Pathol. Pharmakol.* **114**, 313–326.
- Loewe, S. (1927). Versuch einer allgemeinen Pharmakologie der Arznei-Kombinationen. *Klin. Wochenschr.* **6**, 1078–1085.
- Long, G.V., Stroyakovskiy, D., Gogas, H., Levchenko, E., de Braud, F., Larkin, J., Garbe, C., Jouary, T., Hauschild, A., Grob, J.J., et al. (2014). Combined BRAF and MEK inhibition versus BRAF inhibition alone in melanoma. *N. Engl. J. Med.* **371**, 1877–1888.
- Love, M.I., Huber, W., and Anders, S. (2014). Moderated estimation of fold change and dispersion for RNA-seq data with DESeq2. *Genome Biol.* **15**, 550.
- Lu, W., Hu, Y., Chen, G., Chen, Z., Zhang, H., Wang, F., Feng, L., Pelicano, H., Wang, H., Keating, M.J., et al. (2012). Novel role of NOX in supporting aerobic glycolysis in cancer cells with mitochondrial dysfunction and as a potential target for cancer therapy. *PLoS Biol.* **10**, e1001326.
- McKinney, W. (2010). Data structures for statistical computing in python, Proceedings of the 9th Python in Science Conference, pp. 51–56.
- Oliphant, T.E. (2006). *Guide to NumPy* (CreateSpace Independent Publishing Platform).
- Palmer, A.C., and Sorger, P.K. (2017). Combination. *Cell* **171**, 1678–1691.e13.
- Parmenter, T.J., Kleinschmidt, M., Kinross, K.M., Bond, S.T., Li, J., Kaadige, M.R., Rao, A., Sheppard, K.E., Hugo, W., Pupo, G.M., et al. (2014). Response of BRAF-mutant melanoma to BRAF inhibition is mediated by a network of transcriptional regulators of glycolysis. *Cancer Discov.* **4**, 423–433.
- Paudel, B.P., Harris, L.A., Hardeman, K.N., Abugable, A.A., Hayford, C.E., Tyson, D.R., and Quaranta, V. (2018). A nonquiescent “idling” population state in drug-treated, BRAF-mutated melanoma. *Biophys. J.* **114**, 1499–1511.
- Salvatier, J., Wiecki, T.V., and Fonnesbeck, C. (2016). Probabilistic programming in Python using PyMC3. *PeerJ Comput. Sci.* **2**, e55.
- Schiffmann, I., Greve, G., Jung, M., and Lübbert, M. (2016). Epigenetic therapy approaches in non-small cell lung cancer: update and perspectives. *Epigenetics* **11**, 858–870.
- Schindler, M. (2017). Theory of synergistic effects: hill-type response surfaces as “null-interaction” models for mixtures. *Theor. Biol. Med. Model.* **14**, 15.
- Shaw, A.T., Kim, D.W., Mehra, R., Tan, D.S., Felip, E., Chow, L.Q., Camidge, D.R., Vansteenkiste, J., Sharma, S., De Pas, T., et al. (2014). Ceritinib in ALK -Rearranged non-small-cell lung cancer. *N. Engl. J. Med.* **370**, 1189–1197.

- Shimoyama, Y., Nagafuchi, A., Fujita, S., Gotoh, M., Takeichi, M., Tsukita, S., and Hirohashi, S. (1992). Cadherin dysfunction in a human cancer cell line: possible involvement of loss of alpha-catenin expression in reduced cell-cell adhesiveness. *Cancer Res.* 52, 5770–5774.
- Soria, J.C., Ohe, Y., Vansteenkiste, J., Reungwetwattana, T., Chewaskulyong, B., Lee, K.H., Dechaphunkul, A., Imamura, F., Nogami, N., Kurata, T., et al. (2018). Osimertinib in untreated EGFR -mutated advanced non-small-cell lung cancer. *N. Engl. J. Med.* 378, 113–125.
- Subramanian, A., Narayan, R., Corsello, S.M., Peck, D.D., Natoli, T.E., Lu, X., Gould, J., Davis, J.F., Tubelli, A.A., Asiedu, J.K., et al. (2017). A next generation connectivity map: L1000 platform and the first 1,000,000 profiles. *Cell* 171, 1437–1452.e17.
- Tallarida, R.J. (2011). Quantitative methods for assessing drug synergism. *Genes Cancer* 2, 1003–1008.
- Tange, O. (2011). GNU parallel: the command-line power tool. *Login* 36, 42–47.
- Twarog, N.R., Stewart, E., Hammill, C.V., and Shelat, A.A. (2016). BRAID: A unifying paradigm for the analysis of combined drug action. *Sci. Rep.* 6, 25523.
- Tyson, D.R., Garbett, S.P., Frick, P.L., and Quaranta, V. (2012). Fractional proliferation: a method to deconvolve cell population dynamics from single-cell data. *Nat. Methods* 9, 923–928.
- van der Walt, S., Schönberger, J.L., Nunez-Iglesias, J., Boulogne, F., Warner, J.D., Yager, N., Gouillart, E., and Yu, T.; scikit-image contributors (2014). Scikit-image: image processing in Python. *PeerJ* 2, e453.
- Welm, B.E., Dijkgraaf, G.J., Bledau, A.S., Welm, A.L., and Werb, Z. (2008). Lentiviral transduction of mammary stem cells for analysis of gene function during development and cancer. *Cell Stem Cell* 2, 90–102.
- Witta, S.E., Gemmill, R.M., Hirsch, F.R., Coldren, C.D., Hedman, K., Ravdel, L., Helfrich, B., Dziadziszko, R., Chan, D.C., Sugita, M., et al. (2006). Restoring E-cadherin expression increases sensitivity to epidermal growth factor receptor inhibitors in lung cancer cell lines. *Cancer Res.* 66, 944–950.
- Witta, S.E., Jotte, R.M., Konduri, K., Neubauer, M.A., Spira, A.I., Ruxer, R.L., Varella-Garcia, M., Bunn, P.A., and Hirsch, F.R. (2012). Randomized phase II trial of erlotinib with and without entinostat in patients with advanced non-small-cell lung cancer who progressed on prior chemotherapy. *J. Clin. Oncol.* 30, 2248–2255.
- Yadav, B., Wennerberg, K., Aittokallio, T., and Tang, J. (2015). Searching for drug synergy in complex dose-response landscapes using an interaction potency model. *Comp. Struct. Biotechnol. J.* 13, 504–513.
- Zimmer, A., Katzir, I., Dekel, E., Mayo, A.E., and Alon, U. (2016). Prediction of multidimensional drug dose responses based on measurements of drug pairs. *Proc. Natl. Acad. Sci. U S A* 113, 10442–10447.

STAR★METHODS**KEY RESOURCES TABLE**

REAGENT or RESOURCE	SOURCE	IDENTIFIER
Chemicals, Peptides, and Recombinant Proteins		
Trizol	Invitrogen	15596026
DMSO	Sigma	D8418
FBS	Gibco	10437-028
PBS	Corning	21-040-CV
DMEM	Gibco	11965-092
RPMI	Corning	10-040-CV
TrypLE	Gibco	12604-013
DMEM/F12	Gibco	11330-032
SytoxGreen	ThermoFisher	S7020
5-Iodotubericidin	ENZO	EI-293
Abexinostat (PCI-24781)	SelleckChem	S1090
Acetylcysteine	SelleckChem	S1623
Afatinib (BIBW2992)	LC Laboratories	A8644
AG-879	ENZO	EI-258
Alisertib (MLN8237)	MedChemExpress	HY-10971
Amiodarone HCl	SelleckChem	S1979
Aprepitant	SelleckChem	S1189
Bazedoxifene HCl	SelleckChem	S2128
Beclomethasone dipropionate	Light Biologicals (NIH Clinical Collection II)	MZ-3012
Bendroflumethiazide	Light Biologicals (NIH Clinical Collection II)	B-8008
BML-259	ENZO	EI-344
Bosutinib (SKI-606)	LC Laboratories	B-1788
Brigatinib (AP26113)	SelleckChem	S8229
Buparlisib (BKM120, NVP-BKM120)	SelleckChem	S2247
Cabozantinib	LC Laboratories	C-8901
Carfilzomib	LC Laboratories	C-3022
Carmustine	NCI Chemotherapeutic Agents Repository	409962
Cephalomannine	SelleckChem	S2408
Ceritinib (LDK378)	SelleckChem	S7083
Cisplatin	Sigma	470306
Cobimetinib	MedChemExpress	HY-13064
Crizotinib	LC Laboratories	C-7900
Dabrafenib	LC Laboratories	D-5678
Dactolisib	LC Laboratories	N-4288
Dasatinib	LC Laboratories	D-3307
Docetaxel	SelleckChem	S1148
Dronedarone HCl (Multaq)	SelleckChem	S2114
Ensartinib (X-396)	SelleckChem	S8230
Entinostat (MS-275)	SelleckChem	S1053
Erlotinib	LC Laboratories	E-4007
Everolimus (RAD001)	LC Laboratories	E-4040

(Continued on next page)

Continued

REAGENT or RESOURCE	SOURCE	IDENTIFIER
Foretinib (GSK1363089)	SelleckChem	S1111
Gefitinib (ZD1839)	LC Laboratories	G-4408
Givinostat (ITF2357)	SelleckChem	S2170
GSK1751853A	GSK PKIS	N/A
GSK994854A	GSK PKIS	N/A
GW458787A	GSK PKIS	N/A
GW644007X	GSK PKIS	N/A
GW694590A	GSK PKIS	N/A
GW770249X (GW770249A)	GSK PKIS	N/A
Homoharringtonine (Omacetaxine mepesuccinate)	Sequoia Research Products Ltd. (NIH Clinical Collection II)	SRP02125h
Ivacaftor (VX-770)	SelleckChem	S1144
(+)-JQ1	SelleckChem	S7110
Linsitinib (OSI-906)	SelleckChem	S1091
Loratadine	SelleckChem	S1358
LY294002	ENZO	ST-420
M344	SelleckChem	S2779
Methotrexate	MedChemExpress	OL-14377
MG-132	SelleckChem	S2619
ML-9-HCl	ENZO	EI-153
Mocetinostat (MGCD0103)	SelleckChem	S1122
Naftopidil	SelleckChem	S2126
Nateglinide	SelleckChem	S2489
Nebivolol HCl	SelleckChem	S1549
Olaparib (AZD2281, Ku-0059436)	LC Laboratories	O-9201
Osimertinib (AZD9291)	SelleckChem	S7297
Paclitaxel	Sigma	17191
Panobinostat	NCI Chemotherapeutic Agents Repository	761190
2'-Amino-3'-methoxyflavone	LC Laboratories	P-4313
Pimobendan	SelleckChem	S1550
PLX-4720	SelleckChem	S1152
Ponatinib (AP24534)	LC Laboratories	P-7022
PP2	ENZO	EI-297
Pracinostat (SB939)	SelleckChem	S1515
Primaquine Diphosphate	SelleckChem	S4237
Quercetin	ENZO	AC-1142
Quisinostat (JNJ-26481585)	SelleckChem	S1096
RAF-265	MedChemExpress	HY-10248
Rapamycin (Sirolimus)	SelleckChem	S1039
SB-253226	GSK PKIS	N/A
Selumetinib (AZD-6244)	LC Laboratories	S-4490
SP 600125	ENZO	EI-305
Sunitinib Malate	SelleckChem	S1042
TAK-632	SelleckChem	S7291
Tanespimycin (17-AAG)	SelleckChem	S1141
Thioridazine hydrochloride	SelleckChem	S5563
Trametinib	LC Laboratories	T8123
AG-370	ENZO	EI-229

(Continued on next page)

Continued

REAGENT or RESOURCE	SOURCE	IDENTIFIER
U-0126	ENZO	EI-282
Ulixertinib (BVD-523, VRT752271)	SelleckChem	S7854
Vemurafenib (PLX4032)	SelleckChem	S1267
Verteporfin	SelleckChem	S1787
Vindesine	Sequoia Research Products Ltd. (NIH Clinical Collection)	SRP01038v
Vinorelbine Tartrate	SelleckChem	S4269
ZM 447439	SelleckChem	S1103
Critical Commercial Assays		
Tru-Seq stranded mRNA sample prep kit	Illumina	Cat # RS-122-2101
Reverse Transcription Kit	QuantiTect	Cat # 205311
IQTM SYBR Green Supermix	BioRad	Cat # 170
Deposited Data		
Fitted combination surface plots	This Paper	https://github.com/QuLab-VU/MuSyC_Cell.git ; In folder(s): Code_Paper_Figures/Fig2(3).html
Code for Generating Paper Plots	This Paper	https://github.com/QuLab-VU/MuSyC_Cell.git ; In folder(s): Code_Paper_Figures/
Table of fitted parameters for all experiments	This Paper	https://github.com/QuLab-VU/MuSyC_Cell.git ; In folder: Data; Files: MasterResults.csv and MasterResults_plx_dpi_melPanel
RT-qPCR quantification of NOX5 expression	This Paper	https://github.com/QuLab-VU/MuSyC_Cell.git ; In file: Data/nox5Expr.csv
DIP Rate Calculations	This Paper	https://github.com/QuLab-VU/MuSyC_Cell.git ; In folder(s): Data; Files: HTS018_rates, HTS022_timeavg_rates_sub2.csv, -03-27-2018-dpi+plx-cm_bp_timeavg_preCalcDIP_timSub.csv, dasatinib_osimertinib_cellavista_cm_8-24-17.csv, linsitinib_osimertinib_cellavista_cm_8-24-17.csv, HTS015_017_Combined.csv
cFP Raw Data	This Paper	https://github.com/QuLab-VU/MuSyC_Cell.git ; In folder(s): Data/SKME5_cFP
List of DEGS	This Paper	https://github.com/QuLab-VU/MuSyC_Cell.git ; In folder(s): Data/DEGs_GO_Analysis
Raw RNAseq data for subclones	GEO	GEO: GSE122041
This data is also available from Mendeley Data at the following doi	This Paper	[https://doi.org/10.17632/n8bp8db5ff.1]
Experimental Models: Cell Lines		
PC9-H2B.RFP	Tyson et. al. (2012) (W. Pao at UPenn)	N/A
SKMEL5-H2B.RFP	Paudel et al. (2018) (ATCC)	HTB-70
WM1799-H2B.RFP	Paudel et al. (2018) (M. Herlyn at Wistar Institute)	N/A
WM983B-H2B.RFP	Paudel et al. (2018) (M. Herlyn at Wistar Institute)	N/A
A375-H2B.RFP-FUCCI	Paudel et al. (2018) (ATCC)	CRL-1619
SKMEL28-H2B.RFP-FUCCI	Paudel et al. (2018) (ATCC)	HTB-72

(Continued on next page)

Continued

REAGENT or RESOURCE	SOURCE	IDENTIFIER
WM2664-H2B.RFP	Paudel et al. (2018) (M. Herlyn at Wistar Institute)	N/A
A2058-H2B.RFP	Paudel et al. (2018) (ATCC)	CRL-11147
SKMEL5.SC10-H2B.RFP	Paudel et al. (2018) Derived Subclone from SKMEL5-H2B.RFP	N/A
SKMEL5.SC07-H2B.RFP	Paudel et al. (2018) Derived Subclone from SKMEL5-H2B.RFP	N/A
SKMEL5.SC01-H2B.RFP	Paudel et al. (2018) Derived Subclone from SKMEL5-H2B.RFP	N/A
Oligonucleotides		
NOX5_Foward Primer: GGCTCAAGTCCTACCACTGGAA	This paper	N/A
NOX5_Reverse Primer: GAACCGTGTACCCAGCCAAT	This paper	N/A
HPRT_Foward Primer: TGCTCGAGATGTGATGAAGGAG	This paper	N/A
HPRT_Reverse Primer: TGATGTAATCCAGCAGGTCAGC	This paper	N/A
36B4_Foward Primer: CATGTTGCTGGCCAATAAGG	This paper	N/A
36B4_Reverse Primer: TGGTGATAACCTAAAGCCTGGAA	This paper	N/A
PGC1a_Foward Primer: TGCCCTGGATTGTTGACATGA	This paper	N/A
PGC1a_Reverse Primer: TTTGTCAGGCTGGGGTAGG	This paper	N/A
Recombinant DNA		
pHIV-H2B-mRFP	Addgene, Welm et al. (2008)	Plasmid #:18982
Software and Algorithms		
Scikit-learn	Van der Walt et al. (2014)	N/A
RabbitMQ/Celery	www.celeryproject.org	N/A
GNU parallel	Tange (2011)	N/A
Scipy	Jones et al. (2001)	N/A
Matplotlib	Hunter (2007)	N/A
Pandas	McKinney (2010)	N/A
Numpy	Oliphant (2006)	N/A
Pymc3	Salvatier et al. (2016)	N/A
HISAT2	Kim et al. (2015)	N/A
featureCounts	Liao et al. (2014)	N/A
Bioconductor (R)	www.bioconductor.org	N/A
ENRICHR (R)	Kuleshov et al. (2016)	N/A
DESeq2	Love et al. (2014).	N/A

CONTACT FOR REAGENT AND RESOURCE SHARING

Further information and requests for resources and reagents should be directed to and will be fulfilled by the Lead Contact, Vito Quaranta (vito.quaranta@vanderbilt.edu).

EXPERIMENTAL MODEL AND SUBJECT DETAILS

PC9 (previously PC-14, gender unknown) cells were obtained from W. Pao (U Penn.) and were cultured in RPMI 1640 medium containing 10% FBS at 37°C and 5% CO₂. Cells were engineered to express histone 2B-mRFP via lenti-viral transfection using the pHIV-H2B-mRFP plasmid (Welm et al., 2008) as previously described (Tyson et al., 2012). A single-cell derived clonal population demonstrated to exhibit proliferation characteristic of the parental population was then selected by limiting dilution. BRAFV600-mutant melanoma lines cells (A2058 (M), WM1799 (U), A375 (F), WM983B (M), SKMEL5 (F), SKMEL28 (M), WM2664 (F), M=Male, F=Female, U=Unknown) were obtained from ATCC or M. Herlyn (Wistar Institute)(see [Key Resources Table](#)) and were cultured in DMEM media containing 2 mM glutamine, 4.5 g/L glucose, 10% FBS and no sodium pyruvate (catalog 11965-092) as previously

described (Hardeman et al., 2017). SKMEL5.SC10, SKMEL5.SC07, and SKMEL5.SC01 are single cell-derived subclones from SKMEL5 (Paudel et al., 2018). Cell lines were tested for mycoplasma before each experiment.

METHODS DETAILS

Key Equations

For full derivation of these equations, see subsection 4 *Derivation of generalized 2-dimensional hill equation*. This section is meant to serve as a quick reference guide for the main equations used in the paper.

If the behavior of the drugs in the model formulation of Figure S1B obey detailed balance, then the effect of the combination (i.e., the height of combination surface) is described by

$$E_d = \frac{C_1^{h_1} C_2^{h_2} E_0 + d_1^{h_1} C_2^{h_2} E_1 + C_1^{h_1} d_2^{h_2} E_2 + (\alpha_2 d_1)^{h_1} d_2^{h_2} E_3}{C_1^{h_1} C_2^{h_2} + d_1^{h_1} C_2^{h_2} + C_1^{h_1} d_2^{h_2} + (\alpha_2 d_1)^{h_1} d_2^{h_2}}, \quad (\text{Equation 1})$$

where E_d represents the expected effect for a given dose pair d_1, d_2 and is specified with 9 parameters defined in Table S1. In addition, detailed balance enforces the constraint that

$$\alpha_1^{h_2} = \alpha_2^{h_1}. \quad (\text{Equation 2})$$

α is a unitless scalar transforming dose d into an effective dose $\alpha \cdot d$ and is used to quantify synergistic potency in MuSyC.

Synergistic efficacy (β) is calculated from E_0, E_1, E_2, E_3 . β is defined in Equation 3 and is interpreted as the percent increase in maximal efficacy of the combination over the most efficacious single agent. The observed β at the maximum of tested concentrations is defined in Equation 4.

$$\beta = \frac{\min(E_1, E_2) - E_3}{E_0 - \min(E_1, E_2)} \quad (\text{Equation 3})$$

$$\beta_{obs} = \frac{\min[E_1(d1_{max}), E_2(d2_{max})] - E_3(d1_{max}, d2_{max})}{E_0 - \min[E_1(d1_{max}), E_2(d2_{max})]} \quad (\text{Equation 4})$$

Equation 1 can be re-written to include β explicitly by replacing E_3 with $\min(E_1, E_2) - \beta * (E_0 - \min(E_1, E_2))$ resulting in the following equation.

$$E_d = \frac{C_1^{h_1} C_2^{h_2} E_0 + d_1^{h_1} C_2^{h_2} E_1 + C_1^{h_1} d_2^{h_2} E_2 + (\alpha_2 d_1)^{h_1} d_2^{h_2} (\min(E_1, E_2) - \beta * (E_0 - \min(E_1, E_2)))}{C_1^{h_1} C_2^{h_2} + d_1^{h_1} C_2^{h_2} + C_1^{h_1} d_2^{h_2} + (\alpha_2 d_1)^{h_1} d_2^{h_2}} \quad (\text{Equation 5})$$

For drugs that do not follow detailed balance, we have derived a more general formulation with 12 parameters:

$$E_d = [E_0 \ E_1 \ E_2 \ E_3] \cdot \begin{bmatrix} -(r_1 d_1^{h_1} + r_2 d_2^{h_2}) & r_{-1} & r_{-2} & 0 \\ r_1 d_1^{h_1} & -\left(r_{-1} + r_2 (\alpha_1 d_2)^{h_2}\right) & 0 & r_{-2} \\ r_2 d_2^{h_2} & 0 & -\left(r_1 (\alpha_2 d_1)^{h_1} + r_{-2}\right) & r_{-1} \\ 1 & 1 & 1 & 1 \end{bmatrix}^{-1} \cdot \begin{bmatrix} 0 \\ 0 \\ 0 \\ 1 \end{bmatrix} \quad (\text{Equation 6})$$

where again E_3 can be replaced to include β explicitly.

Because we do not know *a priori* whether combinations will follow detailed balance, we use an information theoretic approach to pick the best model for the data. We have defined six tiers of model complexity, and the best model is selected based on minimizing the deviance information criterion. (See section Quantification and Statistical Analysis, subsection 1 *Fitting Dose-response Surfaces* for description of fitting algorithm and Table S5 for description of model tiers).

Comparison to Alternative Synergy Models

Several other methods for calculating synergy exist, including long-standing traditional methods Loewe (Loewe and Muischnek, 1926; Loewe, 1927), Bliss (Bliss, 1939), HSA (Gaddum, 1940; Greco et al., 1995), and CI (Chou and Talalay, 1984), as well as more recent methods such as ZIP (Yadav et al., 2015), BRAID (Twarog et al., 2016), the effective dose model (Zimmer et al., 2016), and Schindler's Hill-PDE model (Schindler, 2017). All of these methods, as well as our own, define a null surface. Combinations with effects greater than or less than expected based on the null surface are deemed synergistic or antagonistic respectively. These methods broadly use one of two approaches to quantify synergy. Loewe, Bliss, CI, HSA, Schindler's Hill-PDE, and ZIP quantify synergy at every concentration based on how the experimentally measured response deviates from the null surface. BRAID, the effective dose model, and MuSyC provide equations with synergy parameters describing the entire surface which is fit to experimental data using non-linear curve-fitting techniques.

Here, we briefly compare our model to each of these others and show that our model (1) describes distinct combination surfaces, (2) results in synergy parameters which are straight forward to interpret, (3) is not restricted to a special class of effects with bounded

scales, and (4) reduces to many of these other approaches in special cases thereby unifying and generalizing seemingly disparate synergy principles.

The Dose Equivalence Principle: Loewe and CI

The first prevalent foundational principle, established by Loewe ([Loewe and Muischnek, 1926](#)) and subsequently expanded on by CI ([Chou and Talalay, 1984](#)), is the Dose Equivalence Principle. This principle states that for a given effect magnitude E achieved by dose x of drug X alone or dose y of drug Y alone, there exists a constant ratio $R = x/y$ such that using Δx less of drug X can always be compensated for by using $\Delta y = R\Delta x$ more of drug Y. Therefore, the null surface is only defined for combinations whose magnitude of effect is less than the weaker drug's maximal effect. This is because for combination effects greater than the effect of the weakest drug, no amount of the weaker drug can compensate for reducing the dose of the stronger drug.

The resulting null surfaces have linear isoboles. Our model recovers this under the constraint that the two drugs are maximally antagonistic. This can be seen by setting $\alpha=0$, and reducing [Equation 6](#) to

$$(E - E_0) + (E - E_1) \left(\frac{d_1}{\Phi_1} \right)^{h_1} + (E - E_2) \left(\frac{d_2}{\Phi_2} \right)^{h_2} = 0.$$

By this it is easy to see when $h_1 = h_2 = 1$, iso-effect lines $\left(\frac{\partial}{\partial E} = 0 \right)$ are represented by the linear isoboles characteristic of Loewe

Additivity and the CI null models. However, even in this case MuSyC is not limited by the weaker drug, and can therefore extend Loewe's isoboles to any combination doses.

The requirement that $\alpha = 0$ means the Loewe and CI null models assumes infinite potency antagonism ($\alpha_1 = \alpha_2 = 0$). Therefore, combinations with $(0 < \alpha < 1)$ may be deemed synergistic by Loewe or CI. However, these values directly reflect a decrease in potency, and our formulation accurately identifies this as antagonistic. Finally, their null model also ignores the possible effect of hill slopes not equal to 1. For drugs with $h < 1$, they will tend to overestimate synergy, while drugs with $h > 1$ will lead to underestimated synergy ([Figures 5C and 5D](#)). Because their null model relies on such specific assumptions, which are not true for many drugs, it is generally impossible to know whether their results reflect true underlying synergy/antagonism, or simply stem from an inappropriate null surface.

The Multiplicative Survival Principle: Bliss and Effective Dose Model

The other prevalent foundational synergy principle is multiplicative survival, described by Bliss ([Bliss, 1939](#)). Bliss' null model assumes the probability of a cell being unaffected by drug 1 (U_1) is independent of the probability of a cell being unaffected by drug 2 (U_2). From this, the null surface states the probability of being unaffected by both drug 1 and drug 2 in combination is $U_{1,2} = U_1 \cdot U_2$. When there is no potency synergy or antagonism, MuSyC reproduces this behavior in the following manner.

Setting $\alpha_1 = \alpha_2 = 1$, consider the fraction of unaffected cells, U , for each drug in isolation:

$$U_i = \frac{1}{1 + \left(\frac{d_i}{\Phi_i} \right)^{h_i}}.$$

And for the two drugs in combination, solving [Equation 67](#) for U we get

$$U_{1,2} = \frac{1}{1 + \left(\frac{d_1}{\Phi_1} \right)^{h_1} + \left(\frac{d_2}{\Phi_2} \right)^{h_2} + \left(\frac{d_1}{\Phi_1} \right)^{h_1} \left(\frac{d_2}{\Phi_2} \right)^{h_2}}.$$

From this, it is easy to verify that $U_{1,2} = U_1 \cdot U_2$, which is equivalent to Bliss Independence. However, the Bliss method explicitly requires the effect being measured in the combination surface is "percent affected", such as percent of cells killed vs. percent of cells remaining. For drugs which induce different maximum effects, Bliss is unable to account for the difference between being affected by drug 1 (E_1), drug 2 (E_2), and/or both ($E_{1,2}$), and may give unreliable results. Our model addresses this by decoupling the effect of a drug (E_0, E_1, E_2, E_3) and the "percent affected" by a drug ($U, A_1, A_2, A_{1,2}$). If the effect itself is measuring percent (un)affected, that corresponds to the case where $E_0 = 1$, $E_1 = E_2 = E_3 = 0$, in which case MuSyC's null model is identical to Bliss'.

Zimmer et. al. introduced the effective dose model ([Zimmer et al., 2016](#)) as a parameterized version of Bliss, and shares the same null surface. However, while Bliss defines synergy at every concentration independently, the effective dose model introduces a parameter $a_{i,j}$ to quantify synergy, similar to MuSyC's potency synergy (α). The $a_{i,j}$ parameter reflects how the presence of drug i modulates the potency of drug j . However, like Bliss, the effective dose model can only be applied to drug responses where the measured drug effect is "percent affected" thereby implicitly requiring the maximum effect of both drugs and the combination is 100% affected which is commonly not observed in dose-response studies ([Fallahi-Sichani et al., 2013](#)).

ZIP

Like the equivalent dose model ([Zimmer et al., 2016](#)), as well as our potency synergy (α), ZIP ([Yadav et al., 2015](#)) works by quantifying how one drug shifts the potency of the other. ZIP is formulated for arbitrary E_0 and E_{max} ; however, it assumes E_{max} is the same for both drugs, as well as the combination (explicitly $E_1 = E_2 = E_3$). To identify potency shifts, the ZIP method fixes the concentration of one drug, then fits a Hill-equation dose response for the other drug. However, for combinations with efficacy synergy or antagonism, dose responses can have non-Hill, and even non-monotonic shapes. In our data, several drugs displayed this behavior. Because our

method accounts explicitly for efficacy synergy, our surfaces are able to describe such complex drug combination surfaces where ZIP fails.

Furthermore, ZIP calculates synergy at every concentration. This is similar to the approach taken by Bliss, Loewe, and CI, and can be used to find doses which “maximize” the observed synergy. However, quantifying synergy on a dose-by-dose basis confounds synergy of potency and efficacy which emerge only on inspection of the global dose-response surface. Additionally, this dose dependent synergy often leads to ambiguous results about whether a given combination is synergistic or not, as it synergizes at some concentrations, and antagonizes at others (Figure 5A).

BRAID

Like ZIP, BRAID (Twarog et al., 2016) assumes that each drug alone has a sigmoidal dose-response, and constructs a Hill-like equation for the combination. This equation uses a single dose parameter κ which combines the doses of both individual drug. To uniquely solve for κ , this formalism, like Loewe additivity, adds the constraint that a drug in combination with itself must be neither synergistic nor antagonistic. By adjusting κ , BRAID is able to fit complex drug combination surfaces, including non-monotonic responses. Because BRAID fits the whole combination surface using a single parameter, it can be used to make unambiguous statements about whether the combination is synergistic or antagonistic. Nevertheless, BRAID does not account for differences in synergy due to efficacy vs. potency, whereas we find many combinations that are synergistic with respect to one, but antagonistic with respect to the other. Further, the biochemical interpretation of κ is not straightforward. And finally, the BRAID model is unable to fit combination surfaces with synergistic efficacy, as it assumes that the maximum effect of the combination is equal to the maximum effect of the stronger single-drug.

Highest Single Agent (HSA)

HSA, originally proposed by Gaddum (1940) and then revived later by Greco (Greco et al., 1995), is a simple heuristic which argues synergy is any combination effect which exceeds the effect of either single agent. While β is conceptually similar to HSA, β provides a global view of the possible increase in effect rather than a point-by-point dose comparison as done in HSA. Because HSA is calculated at every dose it cannot distinguish between synergistically efficacious combinations and synergistically potent combinations as both will increase the effect at intermediate doses (Figure S2). Additionally, as HSA is only defined on a dose-by-dose basis with no model fit, it is sensitive to the dose range selected.

Schindler 2D-Partial Differential Equation (PDE) Model

Schindler's Hill PDE was derived to impute the dose-response surface from the single dose-response curves alone (Schindler, 2017). Therefore, it does not contain any fit parameters, but rather defines a null surface for which synergy results in deviations in the surface. While Schindler did not specify how to account for these deviations, he postulates some implementation of perturbation theory would be sufficient. Like CI and the Equivalent Dose Model, Schindler's framework requires effects in a range between 0 and 1, based on the assumption that the metric is a percent. Therefore, Schindler cannot be applied to data collected with other types of metrics (e.g., DIP Rates). Additionally, Schindler's maximum effect of the combination (E_3) is set equal to the average of the single drug maximal effect. This allows for smooth transitions between the two single dose-response curves but results in some non-intuitive solutions. For example, if drug 1 has a maximal effect of 50% and drug 2 has a maximal effect of 70% the expected additive effect of the combination in the null model is 60% which is less than the maximal effect of drug 1. Therefore, an effect of 65% in combination, though less than achievable with one drug, is designated synergistic by Schindler.

Sham Experiment

It is common for synergy metrics to examine the special case in which the two drugs being combined are actually the same drug in a so called sham experiment first postulated by Chou (Chou and Talalay, 1984). Famously, Loewe, Combination Index, and other methods based on the Dose Equivalence Principle are sham compliant while Bliss and other methods based on the Multiplicative Survival Principle are not. Because our method distinguishes between two types of synergy, we tested sham compliance for each independently. It is immediately apparent synergistic efficacy is sham compliant in all conditions. This can be observed by substituting $E_1 = E_2 = E_3$, as the maximum effect of the drug remains constant, into the definition for β in Equation 3

$$\beta = \frac{\min(E_1, E_2) - E_3}{E_0 - \min(E_1, E_2)} = 0. \quad (\text{Equation 7})$$

To test the sham compliance of synergistic potency, we can write the full dose response surface as a direct 2D extension of the 1D dose-response curve in Equation 12 by replacing d with $d_1 + d_2$.

$$E_d = \frac{E_m(d_1 + d_2)^h + E_0 C^h}{(d_1 + d_2)^h + C^h} \quad (\text{Equation 8})$$

Our 2D generalization of Equation 12, given by Equation 1 can be rewritten for the case of 2 identical drugs by observing that $C_1 = C_2 = C$, $h_1 = h_2 = h$, and $E_1 = E_2 = E_3 = E_m$, resulting in

$$E_d = \frac{C^{2h} E_0 + d_1^h C^h E_m + C^h d_2^h E_m + (\alpha_2 d_1 d_2)^h E_m}{C^{2h} + d_1^h C^h + C^h d_2^h + (\alpha_2 d_1 d_2)^h}. \quad (\text{Equation 9})$$

Setting Equations 8 and 9 equal to one another, we find

$$\alpha_2 = C^h \frac{(d_1 + d_2)^h - d_1^h - d_2^h}{(d_1 d_2)^h}. \quad (\text{Equation 10})$$

This equality is true when $\alpha_2 = \alpha_1 = 0$ and $h = 1$. This makes sense as our model reduces to Loewe additivity under those conditions, and Loewe additivity was developed to explicitly address the sham-combination case. In conclusion, MuSyC satisfies the sham experiment in all conditions where Loewe is the appropriate model.

Derivation of Generalized 2-Dimensional Hill Equation

One-Dimensional Sigmoidal Dose-Response Curve

In pharmacology, the effect of a drug is usually described by the Hill equation, which arises from the equilibrium of a reversible transformation between an unaffected population (U) and an affected population (A)



Here, $[d]$ is the concentration of the drug, h is the Hill slope, and r_1 and r_{-1} are constants corresponding to its rate of action. Solving for the equilibrium results in

$$\frac{\partial U}{\partial t} = A \cdot r_{-1} - U \cdot r_1 d^h \equiv 0$$

$$\frac{A}{U} = \frac{r_1 d^h}{r_{-1}}.$$

When $d^h = \frac{r_{-1}}{r_1}$, then half the population is affected, and half is unaffected ($A = U$). This dose is the EC50, denoted as $C^h = \frac{r_{-1}}{r_1}$.

Adding the constraint that $U + A = 1$, which states that 100% of the population is either unaffected or affected, we find the classic Hill equation:

$$U = \frac{C^h}{C^h + d^h}.$$

If the unaffected and affected populations differ phenotypically by some arbitrary effect (e.g., proliferation rate), the observed effect over the whole population at dose d of some drug will be a weighted average of the two effects by the percent affected and unaffected. Namely,

$$E_d = U \cdot E_0 + A \cdot E_m,$$

where E_0 is the effect characteristic of the unaffected population, and E_m is the effect characteristic of the affected population. From this we find the final form of a 4-parameter sigmoidal equation describing dose-response due to Hill-kinetics:

$$\frac{E_d - E_m}{E_0 - E_m} = \frac{C^h}{C^h + d^h} \quad (\text{Equation 12})$$

Extending the Mass Action Paradigm to Simple Four-State Model Assuming Detailed Balance

Consider a cell type U that can transition into a “drugged” state A_1 in the presence of drug d_1 and into a different drugged state A_2 in the presence of drug d_2 (Figure S1B). We can write these transitions as



where $[d_i]$ denotes concentration of drug d_i . At equilibrium, the forward and reverse rates of these processes are equal, i.e.,

$$r_1[d_1][U] = r_{-1}[A_1] \quad (\text{Equation 15})$$

$$r_2[d_2][U] = r_{-2}[A_2], \quad (\text{Equation 16})$$

where $[A_i]$ is the population of cell state A_i . Defining Θ_x as the ratio of forward and reverse rates ($\Theta_x \equiv \frac{r_{-x}}{r_x}$) and assuming the system obeys detail balance, we find

$$\frac{[U]}{[A_1]} = \frac{\Theta_1}{[d_1]} \quad (\text{Equation 17})$$

$$\frac{[U]}{[A_2]} = \frac{\Theta_2}{[d_2]}. \quad (\text{Equation 18})$$

Now assume that a fourth state exists, $A_{1,2}$, corresponding to a “doubly” drugged state (Figure S1B). A_1 cells can transition into this state in the presence of drug d_2 and A_2 cells can transition into this state in the presence of drug d_1 . We can write these processes as



Note that without loss of generality, we set the forward rate constant for (19) equal to the same value in (14) multiplied by a factor $\alpha_1 > 0$. Similarly, the rate constant for (20) is the same as in (13) multiplied by a factor $\alpha_2 > 0$. Here α represents how each drug potentiates the action of the other and can be interpreted as a change in the “effective” dose of one drug given the presence of the other. When $\alpha=1$ the effective dose of the first drug is the same given the presence of the second drug. When $\alpha<1$, more of the first drug is required to observe the same effective concentrations due to the presence of the second drug. Finally, when $\alpha>1$ the same concentration of the first drug is effectively increased by the second drug.

Again asserting the system obeys detailed balance at equilibrium, we have

$$\frac{[A_1]}{[A_{1,2}]} = \frac{1}{\alpha_1} \frac{\Theta_2}{[d_2]} \quad (\text{Equation 21})$$

$$\frac{[A_2]}{[A_{1,2}]} = \frac{1}{\alpha_2} \frac{\Theta_1}{[d_1]} \quad (\text{Equation 22})$$

We can derive the relationship between the multiplicative factors α_1 and α_2 by rearranging Equation 17 as

$$[U] = \frac{\Theta_1}{[d_1]} [A_1] \quad (\text{Equation 23})$$

Substituting for $[A_1]$ from Equation 21 gives

$$[U] = \frac{1}{\alpha_1} \frac{\Theta_1}{[d_1]} \frac{\Theta_2}{[d_2]} [A_{1,2}] \quad (\text{Equation 24})$$

Substituting for $[A_{1,2}]$ from Equation 22 gives

$$[U] = \frac{\alpha_2}{\alpha_1} \frac{\Theta_2}{[d_2]} [A_2] \quad (\text{Equation 25})$$

Finally, substituting for $[A_2]$ from Equation 18 gives

$$[U] = \frac{\alpha_2}{\alpha_1} [U] \quad (\text{Equation 26})$$

i.e., $\alpha_1=\alpha_2=\alpha$. Note this equality only holds for systems obeying detailed balance. In general, we do not assume this (See Section 4.4 ‘Generalized derivation without assuming detailed balance’) and α_1 and α_2 are independent (Figure S4). However, assuming detailed balance facilitates in deriving a more intuitive form of the 2D Hill equation (Equation 1) compared to the full form (Equation 6).

Now, we define the total cell count

$$C_T \equiv [U] + [A_1] + [A_2] + [A_{1,2}]. \quad (\text{Equation 27})$$

Substituting for $[A_1]$, $[A_2]$, and $[A_{1,2}]$ from Equations 17, 18, and 24, respectively, gives

$$C_T = [U] + \frac{[d_1]}{\Theta_1} [U] + \frac{[d_2]}{\Theta_2} [U] + \alpha \frac{[d_1]}{\Theta_1} \frac{[d_2]}{\Theta_2} [U]. \quad (\text{Equation 28})$$

Solving for $[U]$ gives

$$[U] = \frac{\Theta_1 \Theta_2 C_T}{\Theta_1 \Theta_2 + [d_1] \Theta_2 + \Theta_1 [d_2] + \alpha [d_1] [d_2]}. \quad (\text{Equation 29})$$

Substituting Equation 29 into Equation 17 and rearranging gives

$$[A_1] = \frac{[d_1] \Theta_2 C_T}{\Theta_1 \Theta_2 + [d_1] \Theta_2 + \Theta_1 [d_2] + \alpha [d_1] [d_2]}. \quad (\text{Equation 30})$$

Similarly, from [Equation 18](#) we get

$$[A_2] = \frac{\Theta_1[d_2]C_T}{\Theta_1\Theta_2 + [d_1]\Theta_2 + \Theta_1[d_2] + \alpha[d_1][d_2]}, \quad (\text{Equation 31})$$

and from [Equation 24](#)

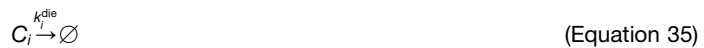
$$[A_{1,2}] = \frac{\alpha[d_1][d_2]C_T}{\Theta_1\Theta_2 + [d_1]\Theta_2 + \Theta_1[d_2] + \alpha[d_1][d_2]}. \quad (\text{Equation 32})$$

As in the derivation of the 1D Hill equation, the measured effect (E_d) is then the relative proportion of cells in each state multiplied by the effect characteristic of that state as in

$$E_d = E_0 * U + E_1 * A_1 + E_2 * A_2 + E_3 * A_{1,2}. \quad (\text{Equation 33})$$

Here we define the effect of each state (E_0, E_1, E_2, E_3) to be proliferation rate in the following way.

We assume that cells in each state can divide and die at rates characteristic of the state, i.e.,



where C_i is specific state of the cell.

We define the drug-induced proliferation (DIP) rate for each state as the difference between the division and death rate constants, i.e.,

$$k_i^{\text{dip}} \equiv k_i^{\text{div}} - k_i^{\text{die}}. \quad (\text{Equation 36})$$

Using [Equation 27](#), the rate of change of the total cell population is

$$\frac{dC_T}{dt} = \frac{d[U]}{dt} + \frac{d[A_1]}{dt} + \frac{d[A_2]}{dt} + \frac{d[A_{1,2}]}{dt}. \quad (\text{Equation 37})$$

From (13), (14), (19), (20), (34)–(36), we get

$$\frac{dC_T}{dt} = k_0^{\text{dip}}[U] + k_1^{\text{dip}}[A_1] + k_2^{\text{dip}}[A_2] + k_3^{\text{dip}}[A_{1,2}]. \quad (\text{Equation 38})$$

Substituting [Equations 29, 30, 31](#), and [32](#) and rearranging, we get

$$\frac{dC_T}{dt} = k_T^{\text{dip}}C_T, \quad (\text{Equation 39})$$

with

$$k_T^{\text{dip}} \equiv \frac{\Theta_1\Theta_2k_0^{\text{dip}} + [d_1]\Theta_2k_1^{\text{dip}} + \Theta_1[d_2]k_2^{\text{dip}} + \alpha[d_1][d_2]k_3^{\text{dip}}}{\Theta_1\Theta_2 + [d_1]\Theta_2 + \Theta_1[d_2] + \alpha[d_1][d_2]}. \quad (\text{Equation 40})$$

Note that with a slight modification, [Equation 40](#) can be written as

$$k_T^{\text{dip}} = \frac{\Theta_1k_0^{\text{dip}} + [d_1]k_1^{\text{dip}} + \frac{\Theta_1[d_2]}{\Theta_2}k_2^{\text{dip}} + \frac{\alpha[d_1][d_2]}{\Theta_2}k_3^{\text{dip}}}{\Theta_1 + [d_1] + \frac{\Theta_1[d_2]}{\Theta_2} + \frac{\alpha[d_1][d_2]}{\Theta_2}}. \quad (\text{Equation 41})$$

Therefore, if $[d_2]=0$ (i.e., single-drug treatment) we get

$$\begin{aligned} k_T^{\text{dip}} &= \frac{\Theta_1k_0^{\text{dip}} + [d_1]k_1^{\text{dip}}}{\Theta_1 + [d_1]} \\ &= \frac{\Theta_1k_0^{\text{dip}} + [d_1]k_1^{\text{dip}} + (\Theta_1k_1^{\text{dip}} - \Theta_1k_1^{\text{dip}})}{\Theta_1 + [d_1]} \\ &= \frac{(\Theta_1 + [d_1])k_1^{\text{dip}} + \Theta_1(k_0^{\text{dip}} - k_1^{\text{dip}})}{\Theta_1 + [d_1]} \\ &= k_1^{\text{dip}} + \frac{\Theta_1}{\Theta_1 + [d_1]}(k_0^{\text{dip}} - k_1^{\text{dip}}). \end{aligned} \quad (\text{Equation 42})$$

Rearranging gives

$$\frac{k_T^{\text{dip}} - k_1^{\text{dip}}}{k_0^{\text{dip}} - k_1^{\text{dip}}} = \frac{\Theta_1}{\Theta_1 + [d_1]}. \quad (\text{Equation 43})$$

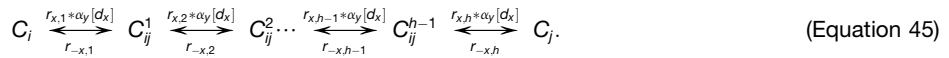
Comparing to [Equation 12](#), we see that [Equation 43](#) is a one-dimensional sigmoidal dose-response curve with $E_d = k_T^{\text{dip}}$, $E_0 = k_0^{\text{dip}}$, $E_m = k_1^{\text{dip}}$, $C = \Theta_1$, and $h=1$. By analogy, we surmise that [Equation 40](#) is a 9 parameter, two-dimensional generalization of [Equation 12](#), i.e.,

$$E_d = \frac{C_1^{h_1} C_2^{h_2} E_0 + d_1^{h_1} C_2^{h_2} E_1 + C_1^{h_1} d_2^{h_2} E_2 + (\alpha_2 d_1)^{h_1} d_2^{h_2} E_3}{C_1^{h_1} C_2^{h_2} + d_1^{h_1} C_2^{h_2} + C_1^{h_1} d_2^{h_2} + (\alpha_2 d_1)^{h_1} d_2^{h_2}}, \quad (\text{Equation 44})$$

with $E_d = k_T^{\text{dip}}$, $E_0 = k_0^{\text{dip}}$, $E_1 = k_1^{\text{dip}}$, $E_2 = k_2^{\text{dip}}$, $E_3 = k_3^{\text{dip}}$, $C_1 = \Theta_1$, $C_2 = \Theta_2$, $h_1=1$, $h_2=1$, and the additional parameter α_2 . Note that under the assumption of detailed balance we found $\alpha_1=\alpha_2$ for the case when $h=1$. Therefore, in the general case when $h \neq 1$, $\alpha_1^{h_2} = \alpha_2^{h_1}$. By fitting the [Equation 44](#), α_1 is uniquely determined.

Four-state model with multiple steps between states

Let us assume instead of occurring in a single step, the cell state transitions are h step processes, i.e.,



Assuming that all steps are in rapid equilibrium, it is straightforward to show that

$$\frac{[C_i]}{[C_j]} = \frac{\prod_{m=1}^h \Theta_{x,m}}{[\alpha_y d_x]^h}, \quad (\text{Equation 46})$$

where $\Theta_{x,m} \equiv r_{-x,m}/r_{x,m}$. Defining $\Phi_x \equiv \sqrt[h]{\prod_{m=1}^h \Theta_{x,m}}$, [Equation 46](#) can be written as

$$\frac{[C_i]}{[C_j]} = \frac{\Phi_x^h}{[\alpha_y d_x]^h}, \quad (\text{Equation 47})$$

which is the well-known Median-Effect Equation from Chou ([Chou, and Talalay, 1983; Chou and Talalay, 1984; Chou, 2010](#)). Replacing reactions (13) and (14) with multi-step processes of the form (45), gives us

$$\frac{[U]}{[A_1]} = \frac{\Phi_1^{h_1}}{[d_1]^{h_1}} \quad (\text{Equation 48})$$

$$\frac{[U]}{[A_2]} = \frac{\Phi_2^{h_2}}{[d_2]^{h_2}}. \quad (\text{Equation 49})$$

Similarly, we replace reactions (19) and (20) with the same multi-step process except with the rate constant for the $C_i \rightarrow C_i^1$ transition (entry into the cascade) equal to $\alpha_y r_{x,1}[d_x]$, giving

$$\frac{[A_1]}{[A_{1,2}]} = \frac{\Phi_2^{h_2}}{[\alpha_1 d_2]^{h_2}} \quad (\text{Equation 50})$$

$$\frac{[A_2]}{[A_{1,2}]} = \frac{\Phi_1^{h_1}}{[\alpha_2 d_1]^{h_1}}. \quad (\text{Equation 51})$$

Note, we assume that the number of steps in the cascade (45) is dependent on the drug type (i.e., $U \rightarrow A_1$ and $A_1 \rightarrow A_{1,2}$, both driven by d_1 , take h_1 steps, while $U \rightarrow A_2$ and $A_1 \rightarrow A_{1,2}$, both driven by d_2 , take h_2 steps). Using [Equations 48, 49, 50, and 51](#) and again defining the total cell count C_T as in [Equation \(27\)](#), we derive

$$[U] = \frac{\Phi_1^{h_1} \Phi_2^{h_2} C_T}{\Phi_1^{h_1} \Phi_2^{h_2} + [d_1]^{h_1} \Phi_2^{h_2} + \Phi_1^{h_1} [d_2]^{h_2} + [\alpha_2 d_1]^{h_1} [d_2]^{h_2}} \quad (\text{Equation 52})$$

$$[A_1] = \frac{[d_1]^{h_1} \Phi_2^{h_2} C_T}{\Phi_1^{h_1} \Phi_2^{h_2} + [d_1]^{h_1} \Phi_2^{h_2} + \Phi_1^{h_1} [d_2]^{h_2} + [\alpha_2 d_1]^{h_1} [d_2]^{h_2}} \quad (\text{Equation 53})$$

$$[A_2] = \frac{\Phi_1^{h_1} [d_2]^{h_2} C_T}{\Phi_1^{h_1} \Phi_2^{h_2} + [d_1]^{h_1} \Phi_2^{h_2} + \Phi_1^{h_1} [d_2]^{h_2} + [\alpha_2 d_1]^{h_1} [d_2]^{h_2}} \quad (\text{Equation 54})$$

$$[A_{1,2}] = \frac{\alpha [d_1]^{h_1} [d_2]^{h_2} C_T}{\Phi_1^{h_1} \Phi_2^{h_2} + [d_1]^{h_1} \Phi_2^{h_2} + \Phi_1^{h_1} [d_2]^{h_2} + [\alpha_2 d_1]^{h_1} [d_2]^{h_2}}. \quad (\text{Equation 55})$$

Therefore, in the same way that we arrived at [Equation 40](#), we can derive

$$k_T^{\text{dip}} \equiv \frac{\Phi_1^{h_1} \Phi_2^{h_2} k_0^{\text{dip}} + [d_1]^{h_1} \Phi_2^{h_2} k_1^{\text{dip}} + \Phi_1^{h_1} [d_2]^{h_2} k_2^{\text{dip}} + [\alpha_2 d_1]^{h_1} [d_2]^{h_2} k_3^{\text{dip}}}{\Phi_1^{h_1} \Phi_2^{h_2} + [d_1]^{h_1} \Phi_2^{h_2} + \Phi_1^{h_1} [d_2]^{h_2} + [\alpha_2 d_1]^{h_1} [d_2]^{h_2}}, \quad (\text{Equation 56})$$

which is of the form [Equation 44](#) with $E_d = k_T^{\text{dip}}$, $E_0 = k_0^{\text{dip}}$, $E_1 = k_1^{\text{dip}}$, $E_2 = k_2^{\text{dip}}$, $E_3 = k_3^{\text{dip}}$, $C_1 = \Phi_1$, and $C_2 = \Phi_2$. From this it is clear the hill coefficient (h) is related to the number of intermediate steps in the system.

The derivation of [Equation 56](#) assumes that the populations of all intermediate cell states C_{ij}^m ($m \in \{1 \dots h - 1\}$) in (45) are small (≈ 0). (This is most evident in our use of [Equation 27](#) for the total cell population, where we only consider the end states. However, it is also implicit in our use of [Equation 46](#), which is used to derive [Equations 52, 53, 54](#), and [55](#) that lead to [Equation 56](#) via [Equation 38](#). In other words, we are assuming that the intermediate states do not significantly contribute to the dynamics of the total cell population. Since it is not reasonable to assume that cells in these states do not divide and die, we must assume the percent occupancy of these states is near zero.) We can satisfy this assumption by requiring that all $r_{x,m}$, $r_{-x,m} \gg 1$ ($m \in \{1 \dots h\}$) and $\Theta_{x,1} \gg \Theta_{x,2} \approx \dots \approx \Theta_{x,h-1} \gg \Theta_{x,h}$. To see this, consider cell state U and all of its intermediate states between states A_1 and A_2 . Let us define

$$U^T \equiv [U] + \sum_{m=1}^{h_1-1} [C_{01}^m] + \sum_{m'=1}^{h_2-1} [C_{02}^{m'}]. \quad (\text{Equation 57})$$

From (45), we see that $\frac{\Theta_{x,1}}{[d_x]} = \frac{[C_{ij}]}{[C_{ij}^1]} \cdot \frac{\Theta_{x,2}}{[d_x]} = \frac{[C_{ij}^1]}{[C_{ij}^2]}$, etc. Therefore,

$$U^T = [U] \left(1 + \frac{[d_1]}{\Theta_{1,1}} + \frac{[d_1]^2}{\Theta_{1,1} \Theta_{1,2}} + \dots + \frac{[d_1]^{h_1-1}}{\prod_{m=1}^{h_1-1} \Theta_{1,m}} + \frac{[d_2]}{\Theta_{2,1}} + \frac{[d_2]^2}{\Theta_{2,1} \Theta_{2,2}} + \dots + \frac{[d_2]^{h_2-1}}{\prod_{m'=1}^{h_2-1} \Theta_{2,m'}} \right). \quad (\text{Equation 58})$$

If $\Theta_{1,1} \gg 1$, $\Theta_{1,m} \ll 1$ ($m \in \{2 \dots h_1 - 1\}$) and $\Theta_{2,1} \gg 1$, $\Theta_{2,m'} \ll 1$ ($m' \in \{2 \dots h_2 - 1\}$), we get $U^T \approx [U]$, i.e., the populations of all intermediate states are ≈ 0 . Now consider cell state A_1 and all of its intermediate states between cell state $A_{1,2}$. Similar to above, we have

$$A_1^T \equiv [A_1] + \sum_{m=1}^{h_2-1} [C_{13}^m] \quad (\text{Equation 59})$$

and

$$A_1^T = [A_1] \left(1 + \frac{\alpha [d_2]}{\Theta_{2,1}} + \frac{[\alpha_1 d_2]^2}{\Theta_{2,1} \Theta_{2,2}} + \dots + \frac{[\alpha_1 d_2]^{h_2-1}}{\prod_{m=1}^{h_2-1} \Theta_{2,m}} \right). \quad (\text{Equation 60})$$

Thus, as before, if $\Theta_{2,1} \gg 1$ and $\Theta_{2,m} \ll 1$ ($m \in \{2 \dots h_2 - 1\}$) we have $A_1^T \approx [A_1]$. However, from (45) we also have

$$\begin{aligned} [A_1] &= \frac{[d_1]}{\Theta_{1,h_1}} [C_{01}^{h_1-1}] \\ &= \frac{[d_1]^{h_1}}{\Theta_{1,1} \Theta_{1,2} \dots \Theta_{1,h_1}} \end{aligned} \quad (\text{Equation 61})$$

Since, from above, $\Theta_{1,1} \gg 1$ and $\Theta_{1,m} \ll 1$ ($m \in \{2 \dots h_1 - 1\}$), we must require that $\Theta_{1,h_1} \ll 1$ and $\Theta_{1,m} \gg 1$ ($m \in \{2 \dots h_1 - 1\}$) in order to offset the large value of $\Theta_{1,1}$ and to ensure that $[A_1] \approx 0$, and to ensure. The latter condition means that $\Theta_{1,m} \approx 1$ ($m \in \{2 \dots h_1 - 1\}$). Therefore, we have the condition that $\Theta_{1,1} \gg \Theta_{1,2} \approx \dots \approx \Theta_{1,h_1-1} \gg \Theta_{1,h_1}$. Similarly, we can derive that $\Theta_{2,1} \gg \Theta_{2,2} \approx \dots \approx \Theta_{2,h_2-1} \gg \Theta_{2,h_2}$ by considering cell state A_2 and all of its intermediate states between cell state $A_{1,2}$ (not shown).

Generalized Derivation without Assuming Detailed Balance

More generally if we do not assume detailed balance, the state occupancy of $U, A_1, A_2, A_{1,2}$ are defined by the partial equilibrium equations

$$\frac{\partial U}{\partial t} = -U \cdot (r_1 d_1 + r_2 d_2) + A_1 \cdot r_{-1} + A_2 \cdot r_{-2} \quad (\text{Equation 62})$$

$$\frac{\partial A_1}{\partial t} = -A_1 \cdot (r_{-1} + \alpha_1 r_2 d_2) + U \cdot r_1 d_1 + A_{1,2} \cdot r_{-2} \quad (\text{Equation 63})$$

$$\frac{\partial A_2}{\partial t} = -A_2 \cdot (\alpha_2 r_1 d_1 + r_{-2}) + U \cdot r_2 d_2 + A_{1,2} \cdot r_{-1} \quad (\text{Equation 64})$$

$$\frac{\partial A_{1,2}}{\partial t} = -A_{1,2} \cdot (r_{-1} + r_{-2}) + A_1 \cdot \alpha_1 r_2 d_2 + A_2 \cdot \alpha_2 r_1 d_1. \quad (\text{Equation 65})$$

A final constraint is

$$U + A_1 + A_2 + A_{1,2} = C_T. \quad (\text{Equation 66})$$

At equilibrium, the Equations 62, 63, 64, and 65 must be equal to zero; however, the system only defines a rank 3 matrix, necessitating Equation 66. Thus we find

$$\begin{bmatrix} -(r_1 d_1 + r_2 d_2) & r_{-1} & r_{-2} & 0 \\ r_1 d_1 & -(r_{-1} + r_2 (\alpha_1 d_2)) & 0 & r_{-2} \\ r_2 d_2 & 0 & -(r_1 (\alpha_2 d_1) + r_{-2}) & r_{-1} \\ 1 & 1 & 1 & 1 \end{bmatrix} \cdot \begin{bmatrix} U \\ A_1 \\ A_2 \\ A_{1,2} \end{bmatrix} = \begin{bmatrix} 0 \\ 0 \\ 0 \\ C_T \end{bmatrix}. \quad (\text{Equation 67})$$

Equations of the form

$$Y \cdot \vec{x} = \vec{b},$$

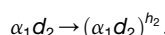
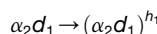
can be solved as

$$\vec{x} = Y^{-1} \cdot \vec{b}.$$

Thus we find the expected effect, as in the 1D case, is the weighted average of the characteristic effect of each state weighted by the state occupancy as governed by the 2D Hill Equation.

$$E = [E_0 \ E_1 \ E_2 \ E_3] \cdot Y^{-1} \cdot \begin{bmatrix} 0 \\ 0 \\ 0 \\ 1 \end{bmatrix}. \quad (\text{Equation 68})$$

This is derived assuming mass action from the reaction rules $U + d \rightarrow A_1 + d$, $A_1 \rightarrow U$. If instead we assume a multi-step transition as in section 4.3, we can simply replace the following in 68



resulting in

$$E_d = [E_0 \ E_1 \ E_2 \ E_3] \cdot \begin{bmatrix} -(r_1 d_1^{h_1} + r_2 d_2^{h_2}) & r_{-1} & r_{-2} & 0 \\ r_1 d_1^{h_1} & -(r_{-1} + r_2 (\alpha_1 d_2)^{h_2}) & 0 & r_{-2} \\ r_2 d_2^{h_2} & 0 & -(r_1 (\alpha_2 d_1)^{h_1} + r_{-2}) & r_{-1} \\ 1 & 1 & 1 & 1 \end{bmatrix}^{-1} \cdot \begin{bmatrix} 0 \\ 0 \\ 0 \\ 1 \end{bmatrix}. \quad (\text{Equation 69})$$

Equation 69 has the following twelve explicit parameters: r_1 , r_{-1} , r_2 , r_{-2} , E_0 , E_1 , E_2 , E_3 , h_1 , h_2 , α_1 and α_2 . There is a relationship defined between a drug's EC_{50} (C in our derivation), the transition rates (r_i , r_{-i}), and the hill slope (h_i), given by $C_i^{h_i} = \frac{r_{-i}}{r_i} | \{i = 1 \text{ or } 2\}$.

Combination Experiments Protocol

Experiments were conducted in the Vanderbilt High Throughput Screening Facility. Cells were seeded at approximately 300 cells per well in 384-well plates and allowed to adhere overnight. A preliminary image of each plate was taken approximately 8 hours after seeding to verify sufficient numbers of cells for each experiment. Images were taken on either the ImageXpress Micro XL (Molecular Devices) or CellVista. The matrix of drug concentrations was prepared using a row-wise and column-wise serial 2X or 4X dilution in

384 well plates using a Bravo Liquid Handling System (Agilent) or manually in 96-well plates. See [Table S2](#) for dose ranges tested. After allowing to adhere overnight, medium containing drugs and 5 nM Sytox Green (to detect dead cells) was added (time = 0) and replaced after 72 hours. Images were obtained at intervals ranging from every 4 to 8 h, depending on the experiment, for >120 hours. Cell counts were determined using custom-image segmentation software developed in Python using scikit-image package ([van der Walt et al., 2014](#)) and run in parallel using RabbitMQ/Celery (<http://www.celeryproject.org/>).

RNA-seq of Melanoma Cell Lines

Total RNA was isolated from untreated SKMEL5 single-cell derived sublines, each in triplicate, using Trizol isolation method (Invitrogen) according to the manufacturer's instructions. RNA samples were submitted to Vanderbilt VANTAGE Core services for quality check, where mRNA enrichment and cDNA library preparation were done with Illumina Tru-Seq stranded mRNA sample prep kit. Sequencing was done at Paired-End 75 bp on the Illumina HiSeq 3000. Reads were aligned to the GRCh38 human reference genome using HISAT2 ([Kim et al., 2015](#)) and gene counts were obtained using featureCounts ([Liao et al., 2014](#)). All downstream analyses were performed in R (<https://www.r-project.org>) using the Bioconductor framework (<https://www.bioconductor.org>)

RT-qPCR Quantification of NOX5 Expression

Total RNA was extracted using Trizol isolation method (Invitrogen) according to the manufacturer's instructions. cDNA synthesis was performed with QuantiTect Reverse Transcription Kit (Cat# 205311) from Qiagen. RT-qPCR was performed using the IQTM SYBR Green Supermix from BioRad (Cat# 1708880). Amplifications were performed in BioRad CFX96 TouchTM Real-Time PCR Detection System. All experiments were done at least in 3+ technical replicates. Log₂ of the transcript expressions were normalized to SKMEL5 subline SC01. HPRT or 36B4 were used as housekeeping gene in all the experiments. Primers used in RT-qPCR are listed in [Key Resources Table](#).

QUANTIFICATION AND STATISTICAL ANALYSIS

Fitting Dose-Response Surfaces

We developed a fitting algorithm, implemented in Python, to fit the combinations experiments to the 2D Hill equation. The fitting is done in three steps, first estimates of the single dose-response parameters (C1,C2,h1,h2,E0,E1,E2) are extracted from fits to the single dose-response curves using the Pythonic implementation of a Levenburg-Marquart (LM) least squares optimization (scipy.optimize.curve_fit). The fit uncertainty (σ) is then the square root of the covariance matrix which is approximated as the inverse of the Hessian matrix (equal to $J^T J$ in LM where J is the Jacobian) at the solution. In the second step, a Particle Swarm Optimizer (10,000 particles, 100 iterations) fits the full 2D Hill equation using the single parameter fits and uncertainties as initial values and bounds ($\pm 2\sigma$). In the last step, the PSO optimized values are used to construct priors for a Metropolis-Hastings Monte-Carlo Markov Chain (MCMC) Optimization (Metropolis Hastings 10,000 iterations). Convergence is tested by checking all parameters' Geweke Z-score. If the Z-score range is (-2,2) over the sampling time frame, the optimization is considered to converge ([Figures S3D and S3E](#)). We found it necessary to use both the PSO and MCMC in order to fit a wide range of dose-response surfaces ([Figure S3](#)). To test the sensitivity of our fitting algorithm, we generated *in silico* data for 125 different dose-response surfaces at different data densities. The density of data tested were square matrixes of rank 5, 7, 10, 15, and 25. At each density 25 different dose-response surfaces were sampled across a 5x5 grid of log(α) and β values ranging from [-2,2] and from [-0.5,0.5], respectively. The parameters for E0, the single drug hill slope, EC50, and maximal effects were held constant at (0.3, 1, 10e-5, and 0.0), respectively. Random noise equal to the average uncertainty in the DIP Rate fits from the NSCLC screen was added to the data (0.001). In all conditions we observed a PSO particle count of 10,000 converged to a minimum in <60 iterations ([Figure S3A](#)). However, this minimum was not the optimal solution. The addition of an MCMC walk further improved fits ([Figure S3B](#)) (Pymc3 package). The MCMC walk calculates the posterior distribution for each parameter from which each parameter's value (mean of trace) and uncertainty (standard deviation of trace) is calculated. Uncertainty in (E0, E1, E2, and E3) was propagated when calculating β using the equation

$$\sigma\beta = \sqrt{\left(\left(\frac{E0 - E3}{(E0 - Ex)^2} * \sigma Ex \right)^2 + \left(\frac{-\sigma E3}{E0 - Ex} \right)^2 + \left(\frac{E3 - Ex}{(E0 - Ex)^2} * \sigma E0 \right)^2 \right)}$$

where Ex and σ Ex are min(E1,E2) and $\sigma(\min(E1,E2))$ respectively. All other uncertainty propagations were handled with python package uncertainties ([Lebigot, 2011](#)). By calculating the uncertainty in the synergy parameters from the posterior distributions, the significance of synergy can be assessed in an unbiased way. Multiple factors contribute to increasing uncertainty in the fitted parameters. Dose-selection, an important consideration in all drug response profiling, changes the certainty of the fits ([Figures S3C–S3E](#)). While we are unable to observe saturating effects implicit in the model for some of our drug combinations – due to limited solubility or potency of the drug – by keeping careful account of the uncertainty in our synergy calculations we can still interpret the synergy of non-optimal dose-regimes. To demonstrate this, we generated the same 25 dose-response surfaces with varying log(α) and β values ranging from [-2,2] and from [-0.5,0.5] respectively but at different coverage of the dose-response curve. The uncertainty in the synergy parameters increases for decreased dose range ([Figures S3C and S3D](#)). It is important to note that in general the uncertainty is a function of many different aspects other than data density including the hill slope of the single curves (high hill slopes

can result in higher uncertainty in $\log(\alpha)$), noise of experimental data, and quality of priors resulting from the single-drug fits. We posit the rigorous approach taken here accounts for all these sources resulting in a true estimate of confidence in a particular synergy value.

To prevent over fitting the data, we have defined six different model tiers which have increasing degrees of freedom (Table S5). To select the correct model tier, we penalize models with higher degrees of freedom by selecting the model based on minimizing the deviance information criterion (DIC) (Berg et al., 2004). Fits for each nest are used to inform priors for subsequent nests. Only drug combinations which converged to the full model (tier 5 with fits for all 12 parameters – Equation 69 in section 4.4 of Methods Details) were used for subsequent analysis. The MCMC optimization additionally allows for quantification of parameter confidence given the data. The following packages were used for fitting, data analysis, or visualization: GNU parallel (Tange, 2011), SciPy (Jones et al., 2001), Numpy (Oliphant, 2006), Pandas (McKinney, 2010), Matplotlib (Hunter, 2007). Pymc3 (Salvatier et al., 2016).

Calculating the DIP Rate

Traditionally, the efficacy of an anti-proliferative compound is measured as the percent of viable cells (relative to control) after a treatment interval (Fallahi-Sichani et al., 2013); however, it has been recently shown this metric is subject to temporal biases (Hafner et al., 2016 ; Harris et al., 2016). To address these biases, we previously developed an unbiased metric of drug effect termed the drug-induced proliferation (DIP) rate (Harris et al., 2016). The DIP rate is defined as the steady state proliferation rate after drug equilibration. A positive DIP rate indicates an exponentially growing population, while a negative DIP rate indicates a regressing one. A rate of zero indicates a cytostatic effect, which may result from cells entering a non-dividing state or from balanced death and division (Paudel et al., 2018). We used the available findDIP R package for calculating DIP rates from growth curves which automatically selects the interval after drug equilibration (https://github.com/QuLab-VU/DIP_rate_NatMeth2016.git).

Calculating Loewe, CI, Bliss, and HSA

To compare our method to the prevailing methods for computing synergy, we calculated Loewe, CI, Bliss for the data from the osimertinib screen in Figure 2 and melanoma BRAF/MEK data of Figure 3. Loewe is agnostic to effect metric, and so we applied it directly to the DIP rate. To calculate CI and Bliss, we imputed the percent viability at 72 hours from the DIP rate for each condition. Percent viability is defined as in equation 1.

$$\% - \text{viable} = \frac{\text{Cell Count}(t = 72\text{hr}) \text{ Treated}}{\text{Cell Count}(t = 72\text{hr}) \text{ Control}} \quad (\text{Equation 70})$$

Estimates of percent viability are sensitive to even small differences between initial cell counts in the control and treated wells due to exponential amplification (Harris et al., 2016). To correct for this the bias, a 'matching' control cell count at 72-hours for each treated condition was calculated using equation

$$\text{Cell Count}(t = 72\text{hr}) \text{ Control} = (\text{Cell Count}(t = 0\text{hr}) \text{ Treated}) * 2^{\text{Control Growth Rate} * 72\text{hr}} \quad (\text{Equation 71})$$

where Control Growth Rate is the median of the fitted growth rates for all control wells. Because the automated microscope did not image all the conditions at exactly zero or seventy two hours, we extrapolate and interpolate respectively the cell count at these times from the measured time series.

The Bliss metric only requires marginal data. For each experiment, individually, we calculated a Bliss score as

$$\text{Bliss} = PV_1|d_1 * PV_2|d_2 - PV_{1,2}|d_1, d_2 \quad (\text{Equation 72})$$

where $PV_i|d_i$ is the %-viability measured for treatment with drug i alone at dose d_i , and $PV_{1,2}|d_1, d_2$ is the %-viability measured for the combination treatment. The first term corresponds to the expected viability, assuming independence, while the second term is the measured viability. By this definition, $\text{Bliss} > 0$ is synergistic, and $\text{Bliss} < 0$ is antagonistic.

Loewe and CI require parameterization of a 1D Hill equation for each drug alone.

$$E = E_{\max} + \frac{E_0 - E_{\max}}{\left(\frac{d}{C}\right)^h + 1} \quad (\text{Equation 73})$$

CI, as per standard calculations (Chou and Talalay, 1984), further requires that $E_0 = 1$ and $E_{\max} = 0$ and is fit to a linearized, log-transformed version of the hill equation (Chou, 2010) which has been previously critiqued for artificial compression of uncertainty in experimental data leading to poor model fits compared with nonlinear regression (Ashton, 2015). CI dose-response curves were fit using the scipy.stats.linregress module. All data points with percent viability greater than 1 were excluded from the CI fit, as $\log(1 - \text{pervia}/\text{pertia})$ becomes complex. For some drugs, this left too few points to fit a line, such that CI was undefined for combinations with those drugs. In other drugs, the fit hill coefficient was negative, and likewise all CI values were undefined for those drugs. For Loewe, we used the single-drug parameters fit by MuSyC.

From these parameterized hill equations, Loewe and CI were calculated using

$$S = -\log_{10} \left(\frac{d_1}{D_1} + \frac{d_2}{D_2} \right) \quad (\text{Equation 74})$$

where D_i is the amount of drug i which, alone, achieves an effect equal to the combination effect, and is calculated from the Hill equation fit for that drug. We take the negative log to transform the synergy values to match Bliss, such that S>0 is synergistic, while S<0 is antagonistic. Because Loewe allows the two drugs to have different E_{max} , Loewe synergy cannot be calculated for measurements which exceed the weaker drug's E_{max} because no amount of the weaker drug alone would be sufficient to achieve that effect; therefore, those conditions are undefined.

For calculating HSA (Gaddum, 1940), we calculate the difference between the observed effect at each combination concentration and the most efficacious single agent effect at those doses. This difference is integrated across the surface to yield a single value for a particular combination.

Fitting ZIP, BRAID, Schindler's Hill PDE, and Equivalent Dose Models

Theoretical dose-response surfaces with different combinations of synergistic potency and efficacy were generated then fit to estimate the synergy according to these methods (Figure S2). Both ZIP and BRAID were calculated using the R packages available for each method (ZIP's R code is in the supplemental file 1 of the manuscript (Yadav et al., 2015) and BRAID's package is available from: <https://cran.r-project.org/web/packages/braidReports/braidReports.pdf>). Schindler's Hill PDE model contains no fitting parameters as the dose-response surface is derived purely from the marginal data. In fact, Schindler does not propose a method to estimate synergy from experimental data, but postulates some implementation of perturbation theory could be used to fit experimental data (Schindler, 2017). Therefore, to calculate the synergy of this model, we defined the sum of residuals between the null surface and the experimental data to the metric of synergy. Finally, to fit Zimmer et al.'s Equivalent Dose Model we used the curve_fit() module of the scipy.optimize package in python. Specifically, the Equivalent Dose Model, equation 2 in (Zimmer et al., 2016), contains parameters for C1,C2, a12, a21, h1, and h2 where the C parameters are the EC50 of the single agents, the $a_{i,j}$ parameters are the synergy values corresponding to a change in potency, and the h parameters are the hill slopes of the single agents. In the model, there are no parameters for efficacy because it is assumed the drug effect ranges between zero and one. When this is not true, the Effective Dose Model results in poor fits to the data (Figure S2) similar to CI.

Identifying DEGs for GO Enrichment Analysis

Differentially Expressed Genes (DEGs) were selected by ANOVA on baseline gene expression data on three clones based on a statistical cutoff of Likelihood Ratio Test (LRT) (p -values < 0.001). Functional enrichment analyses, including GO Term Enrichment and Pathway Enrichment Analysis were done using CRAN Package "Enrichr" (<https://cran.r-project.org/web/packages/enrichR/index.html>), based on a web-based tool for analyzing gene sets and enrichment of common annotated biological functions (Kuleshov et al., 2016). The enriched GO terms and enriched KEGG pathways were restricted to those with p -values corrected for multiple testing less than 0.001. The top GO Biological Processes included generation of precursor metabolites and energy, electron transport chain, inorganic cation transmembrane transport, and metabolic process. The top GO Molecular Function terms included inorganic cation transmembrane transporter activity, cofactor binding, NAD binding, and ATPase activity. The top GO Cellular Component term was the mitochondria membrane. Top KEGG pathways enriched in the DEGs included metabolic pathways, oxidative phosphorylation, carbon metabolism and TCA cycle (Figure 3B). Overall, these enriched GO terms and pathways point toward differences in the regulators of metabolic function in the three subclones. This is consistent with previous reports that suggest altered metabolism is implicated in drug sensitivity and melanoma resistance to BRAFi (Parmenter et al., 2014; Hardeman et al., 2017).

Correlation of BRAFi insensitivity was computed for each identified DEG according to DIP Rate at 8uM PLX-4720 for a 10 cell line panel (Table S3) Pair-wise comparisons of DEGs was performed on genes (after low count genes were removed) using DESeq2 pipeline (Love et al., 2014).

DATA AND SOFTWARE AVAILABILITY

All raw cell counts, calculated DIP rates, DEGs between subclones, and expression data are available in the github repo: https://github.com/QuLab-VU/MuSyC_Cell.git in the folder Data. Additionally, the repo contains all the code required to reproduce all the figures and supplemental figures from the data and is found in the Code_Paper_Figures folder. The subfolders Fig2 and Fig3 contain html folders with interactive plots of all the screened combinations. Open the .html files using a browser. The raw RNAseq is available from GEO at the accession number GSE122041. The software for interactive manipulation of the different parameters to study their contribution to the contours of the dose-response surface is also available in the github repo in the folder MuSyC_App. This folder contains both the matlab source code and a compiled application for the different operating systems. A copy of the github repo at the time of publication is also available from Mendeley Data via the following <https://doi.org/10.17632/n8bp8db5ff>.

Supplemental Information

Quantifying Drug Combination

Synergy along Potency and Efficacy Axes

Christian T. Meyer, David J. Wooten, B. Bishal Paudel, Joshua Bauer, Keisha N. Hardeman, David Westover, Christine M. Lovly, Leonard A. Harris, Darren R. Tyson, and Vito Quaranta

Supplemental Materials

Quantifying the synergy of drug combinations with respect to potency and efficacy.

Christian T. Meyer^{† 1,3}, David J. Wooten^{† 2,3}, B. Bishal Paudel^{† 4,5}, Joshua Bauer^{4,5,6}, Keisha N. Hardeman^{4,5}, David Westover⁶, Christine M. Lovly^{5,7}, Leonard A. Harris^{3,4}, Darren R. Tyson^{3,4}, and Vito Quaranta * 3,4,8,9

¹Program in Chemical and Physical Biology, Vanderbilt University School of Medicine, Nashville, Tennessee.

²Program in Cancer Biology, Vanderbilt University School of Medicine, Nashville, Tennessee.

³Center for Cancer Systems Biology at Vanderbilt, Vanderbilt University, Nashville, Tennessee.

⁴Department of Biochemistry, Vanderbilt University Nashville, Tennessee.

⁵Vanderbilt Ingram Cancer Center, Vanderbilt University Medical Center, Nashville, Tennessee.

⁶Institute of Chemical Biology, High-Throughput Screening Facility, Vanderbilt University, Nashville, Tennessee.

⁷Department of Medicine, Division of Hematology and Oncology, Vanderbilt University Medical Center, Nashville, Tennessee.

⁸Department of Pharmacology, Vanderbilt University School of Medicine, Nashville, Tennessee.

⁹Lead Contact

*Correspondence should be directed to V.Q. (vito.quaranta@vanderbilt.edu).

†These authors contributed equally to this work.

Contents

1 Supplemental Figures	2
2 Supplemental Tables	10

1 Supplemental Figures

Figure S1: Phenomenological model underlying the Hill equation and corresponding extension to two drug case. Related to Figure 1. A) The Hill equation can be derived for a system of two states with characteristic effects (E_0 and E_1) for which the transition rate, and thereby the equilibrium, between the states is a function of the where d is the drug concentration and h represents the hill coefficient (also known as cooperativity). In our system, E_0 and E_1 are defined by the proliferation rate in minimal and maximal drug concentration (i.e. DIP Rate), represented by the slope of a log-transformed growth curve. Here, the case of an anti-proliferative drug is considered where $E_1 < 0$ indicates maximal concentration of drug induces population regression and $E_0 > 0$ indicating an untreated, expanding population. B) Allostery-inspired extension to a 4-state model of combination drug action used to derive the 2D generalization of the Hill equation. The equilibrium between the percent of cell affected by drug 1 or drug 2 alone (A_1 and A_2 respectively) and the doubly affected (A_{12}) populations is governed by the concentration of drug 1 modulated by α_2 (which quantifies drug 2's action on the potency of drug 1) and by the converse, drug 2 multiplied by α_1 . E_3 represents the maximal effect of the combination. C) Combination surfaces with asymmetric synergistic potency ($\alpha_1 > 1$, $\alpha_2 < 1$). The three surfaces correspond to the following conditions (from left to right): combination with asymmetric potency and no synergistic efficacy ($E_1 = E_2 = E_3$); combination with asymmetric synergistic potency with synergistic efficacy ($\min(E_1, E_2) > E_3$); combination with asymmetric synergistic potency with antagonistic efficacy ($\min(E_1, E_2) < E_3$).

Figure S2: Conflation of synergy of potency and efficacy in current synergy frameworks. Related to Figure 1. A) A survey of Loewe calculations on a range of hypothetical drug combinations across a DSD spanning synergistic to antagonistic potency and efficacy. For each combination of β and $\log(\alpha)$ (where $\alpha = \alpha_1 = \alpha_2$), a corresponding value for Loewe synergy was calculated at the drugs' EC50, resulting in a contour map (see bar above DSD for color legend, white is effect sizes undefined by Loewe, i.e., the effect of the combination is greater than the maximum of either drug alone). Along the contour lines, Loewe synergy values remain the same, indicating conflation of synergistic potency and efficacy. As an example, Loewe calculations yield the same value for drug combinations X and O (0.5); whereas MuSyC reveals that combination X is synergistically potent, while combination O is synergistically efficacious. Complete dose-response surfaces for X and O are also shown to further clarify the resolution of synergistic potency and efficacy by MuSyC (Right panels). B-F) Synergy calculations for other methods show the same conflation of synergy of potency and efficacy. Bliss was also calculated at the combination of each drug at the EC50, otherwise synergy metrics are calculated using the whole surface. See STAR Methods section Quantification and Statistical Analysis for details on synergy calculations. G) Combination Index precludes synergy of efficacy by enforcing the maximum effect of the drug to equal 0. This assumption results in poor fits when Emax does not equal zero which is commonly observed experimentally (e.g., Figure 5E). H) The reduction in fit quality for Combination Index is a monotonically decreasing function of Emax for Emax > 0. I-J) The equivalent dose model (Zimmer et al., 2016) also enforces an Emax of 0 resulting in a fit quality which decreases as Emax increases.

Figure S3: Bayesian synergy parameter estimation in the MuSyC algorithm. Related to STAR Methods. A) A particle swarm optimizer (PSO) was tested for convergence across several different data densities ranging from 5X5 to 25X25 grids. Within each density range, 25 different dose-response surfaces were fit (See STAR Methods section Quantification and Statistical Analysis, subsection Fitting Dose-Response Surfaces, for all parameters used). At all tested densities for all conditions, a minimum in the log-likelihood was observed after approximately 60 iterations. B) Comparison of the error in final fits of the parameters between three methods PSO alone followed by a non-linear least squares (NLLS) optimizer (Levenberg-Marquardt), Markov Chain Monte Carlo (MCMC) posterior estimation, and PSO seeded MCMC optimization. Y-axis is the L2-norm of the fitted parameters to the true parameters. Across all data densities, PSO seeded MCMC had the highest fit accuracy across different dose-response surface topologies. C) Synergy parameter uncertainty as a function of dose coverage. σ is the standard deviation of the MCMC trace. As the dose coverage decreases, there is a commensurate increase in the uncertainty of in the fit across different dose-response surfaces. D) Trace-plots and posterior distributions of $\log(\alpha_1)$, $\log(\alpha_2)$, and E_3 for a surface where max dose is equal to the EC50 (bottom). Red line demarcates the true value. Middle plot is the z-score of 20 segments from the overall sample ordered by trace number. Parameters which have absolute z-scores > 2 at any point in the trace are considered not to have converged. E) Trace-plots and posterior distributions of $\log(\alpha_1)$, $\log(\alpha_2)$, and E_3 .

for a surface where max dose is 10,000 times the EC50 fully capturing the drug effect saturation. Posterior distributions are narrower than for the surface with less coverage corresponding to an increase in uncertainty. However, other factors than dose-selection can contribute to fit uncertainty including experimental noise, density of data, steepness of single drug curves (i.e., the hill coefficient), and quality of priors in the MCMC fit.

Figure S4: Synergistic potency (α_1 , α_2) and efficacy (β) do not depend on the potency and efficacy of the single drugs (C and Emax) and are independent of one another. Related to Figure 2. A) Jitter plot of the 64 surveyed single drug's Emax(obs), C [uM], and hill slope h. B) Synergy parameters do not correlate (Pearson-r) with a single drug's potency and efficacy in isolation. ($\alpha_2=X$ potentiates osimertinib). C) α_1 is independent of α_2 in the NSCLC screen. α_1 vs. α_2 by drug class examining the potentiation of drug X by osimertinib (α_1) and the potentiation of osimertinib by drug X (α_2). Ceritinib is not potentiated by osimertinib (last panel) while osimertinib is potentiated by ceritinib (Figure 2C).

Figure S5: Synergistic potency, synergistic efficacy, and maximal effect of combined RAFi and MEKi. Related to Figure 3. A) Jitter plots of $\log(\alpha_1)$ for each RAFi for the 4 MEKi tested. α_1 corresponds to the alteration in MEKi's effective dose due to the presence of a RAFi. Dashed line denotes zero separating synergistic and antagonistic potency. The color of plotted points corresponds to the cell line as annotated at the bottom of the figure. B) Jitter plots of $\log(\alpha_2)$ for each MEKi for the 4 RAFi tested. α_2 corresponds to the alteration in RAF inhibitor's effective dose due to the presence of a MEK inhibitor. C) Rank ordered jitter plots of the median β_{obs} for each drug combination across all cell lines. D) Distribution of maximal effects for RAFi alone ($E1$, 4 drugs), MEKi alone ($E2$, 4 drugs), and the combination ($E3$, 16 combinations) for each cell line. Orange bar denotes mean.

Figure S6: Errors in Melanoma dataset for other methods. Related to Figure 5. Distribution of synergy calculated by Loewe, CI, and Bliss for melanoma dataset. As in the PC9 data, Loewe was calculated directly from DIP rates, while CI and Bliss were calculated from 72-hour viability. Conditions for which synergy is undefined were not included (See STAR Methods, Section Quantification and Statistical Analysis). By these traditional methods, combinations of BRAF/MEK inhibitors in melanoma are ambiguous, spanning synergy (Syn-gray) and antagonism (Ant-white). $\log(\alpha_1)$ is the RAFi's effect on the potency of the MEKi and $\log(\alpha_2)$ is the reverse. Abbreviations of the RAF inhibitors are: dab=dabrafenib, plx=plx4720, raf=raf265, and vem=vemurafenib.

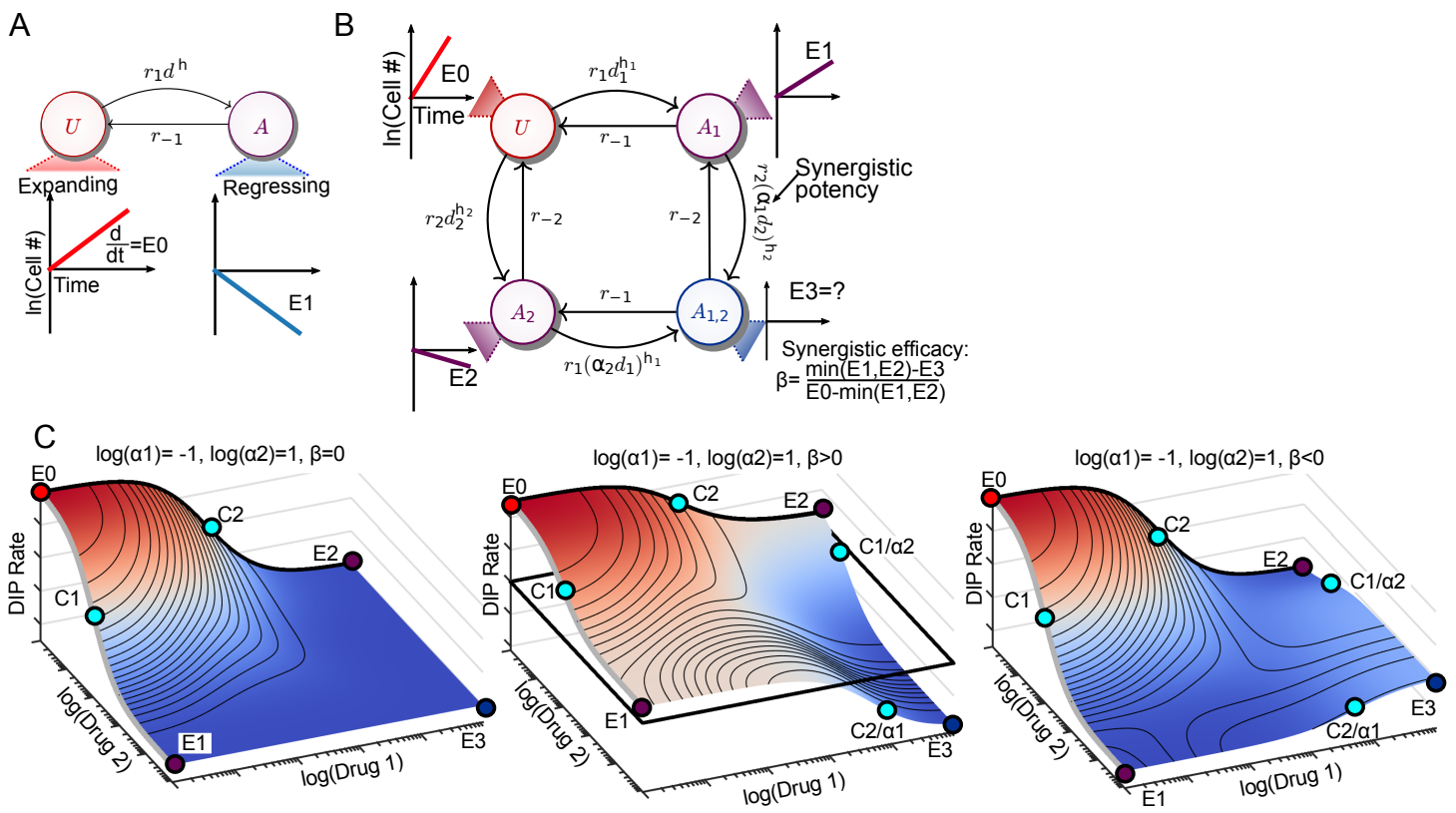


Figure S1

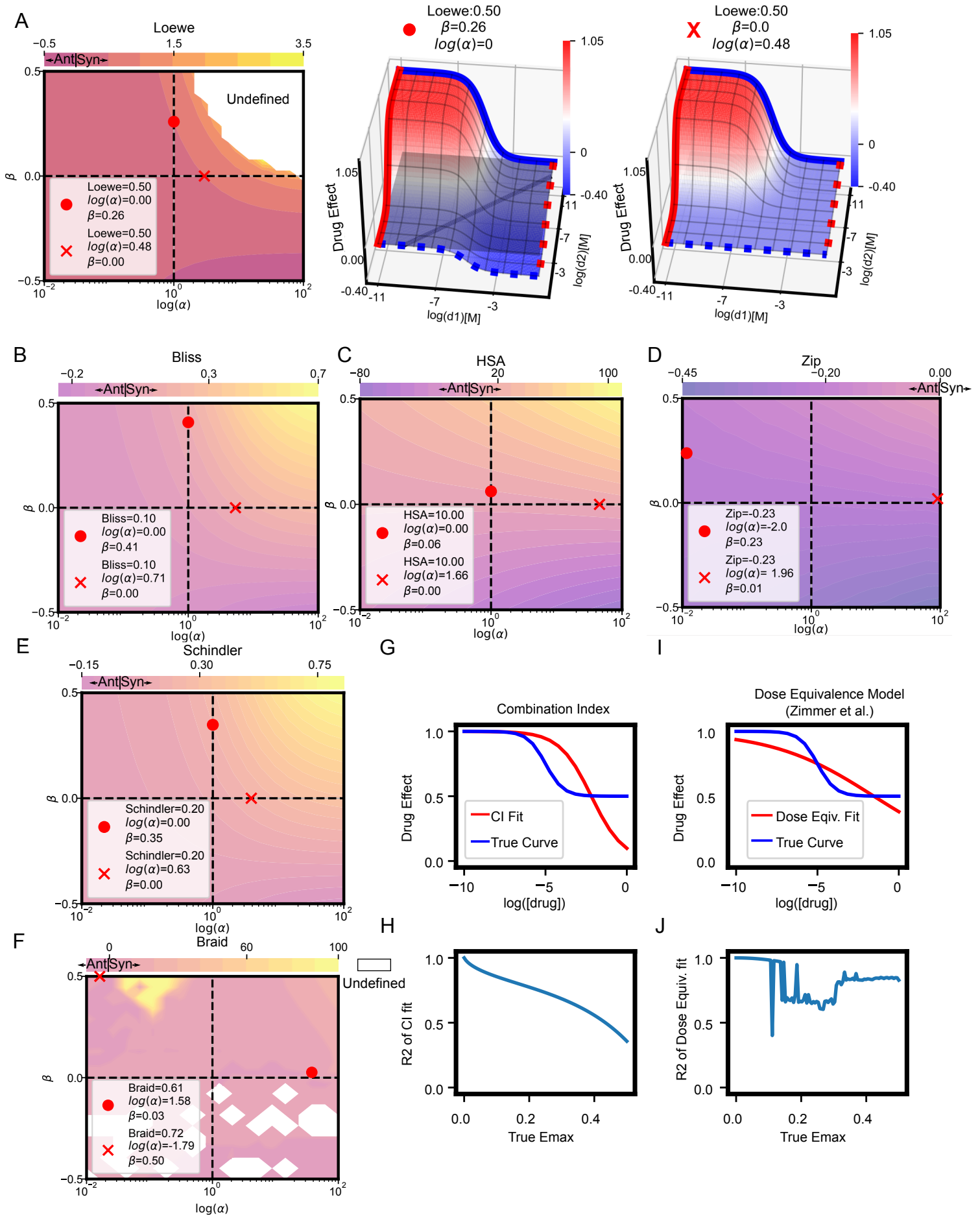


Figure S2

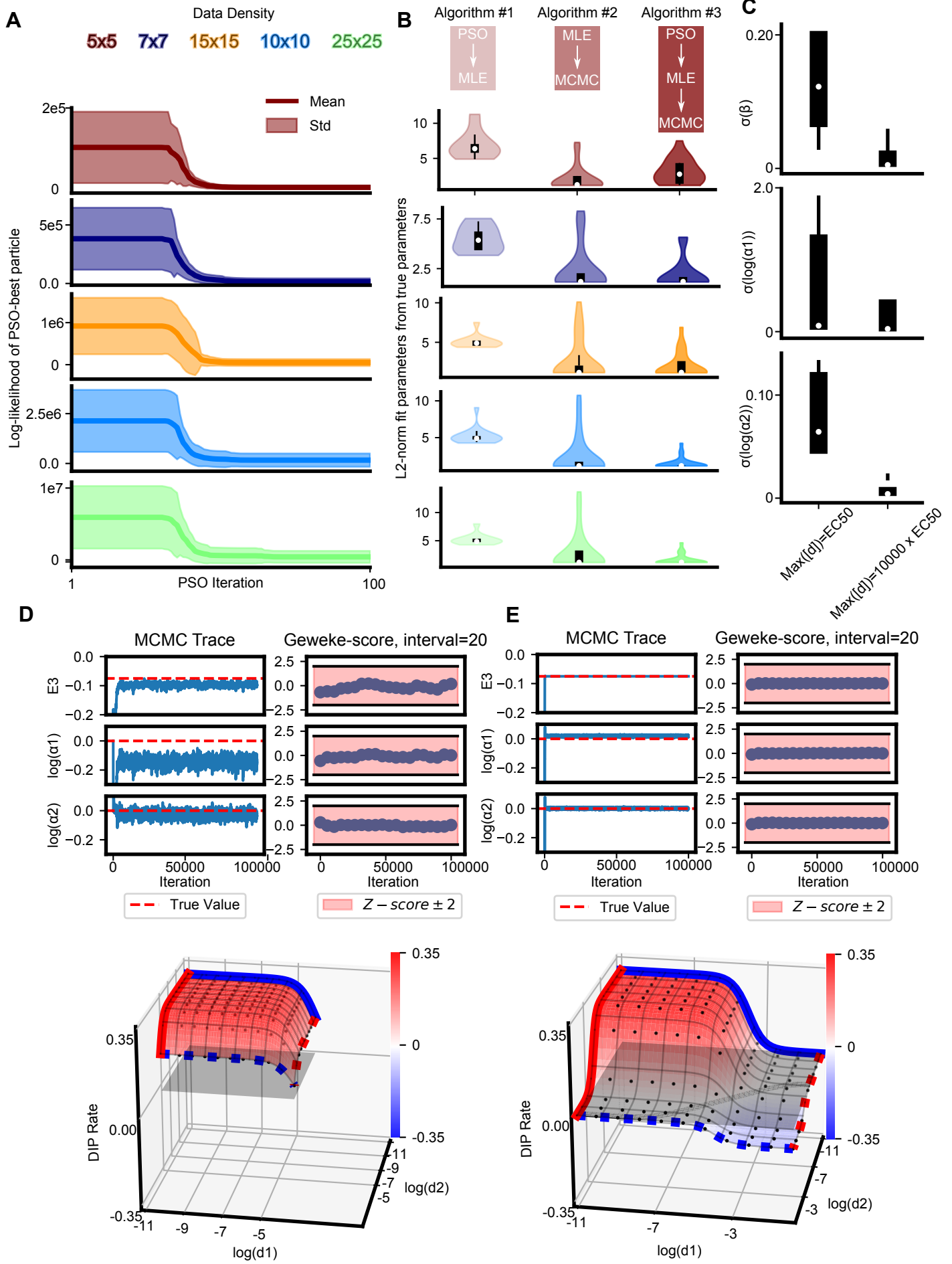


Figure S3

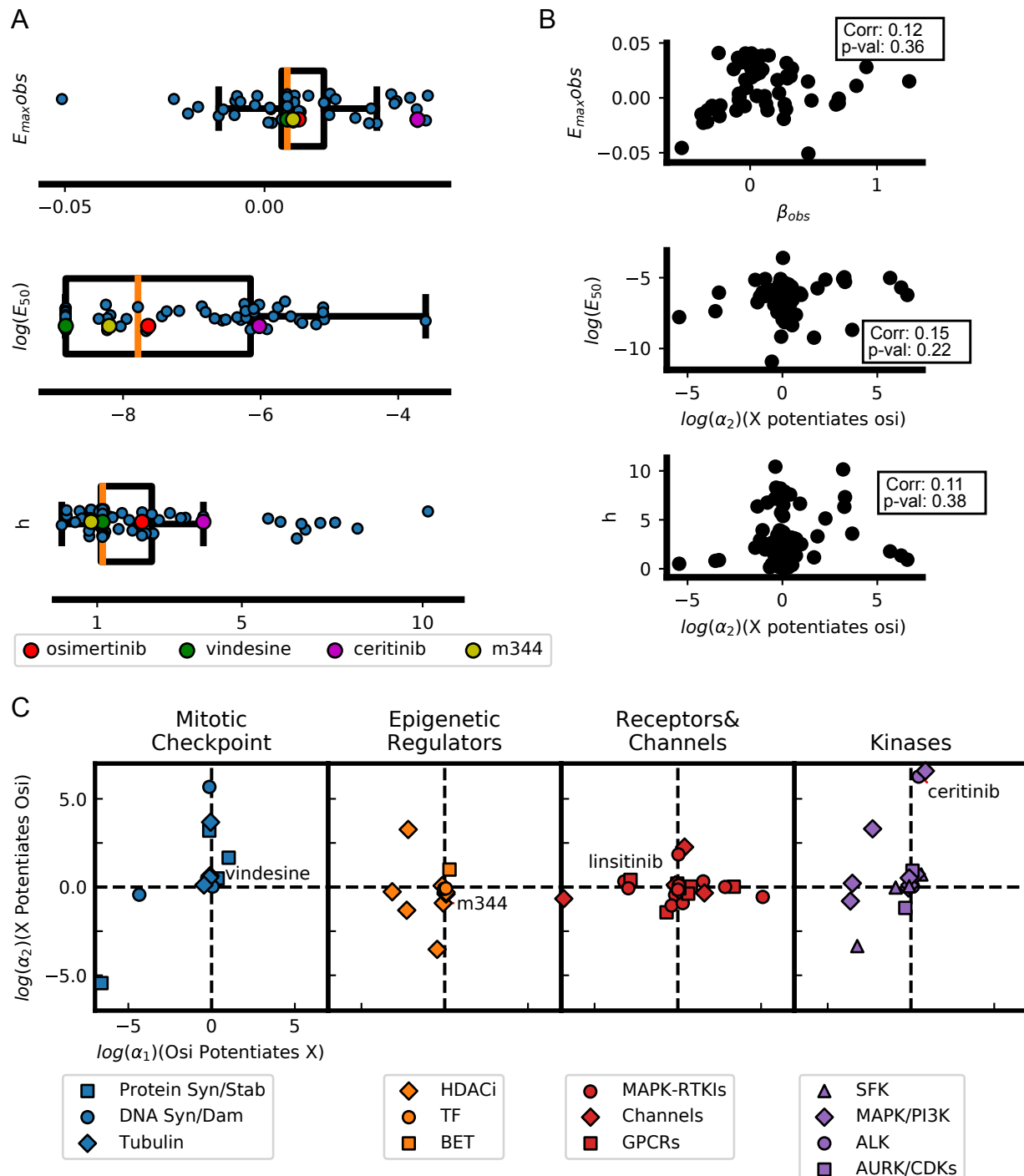


Figure S4

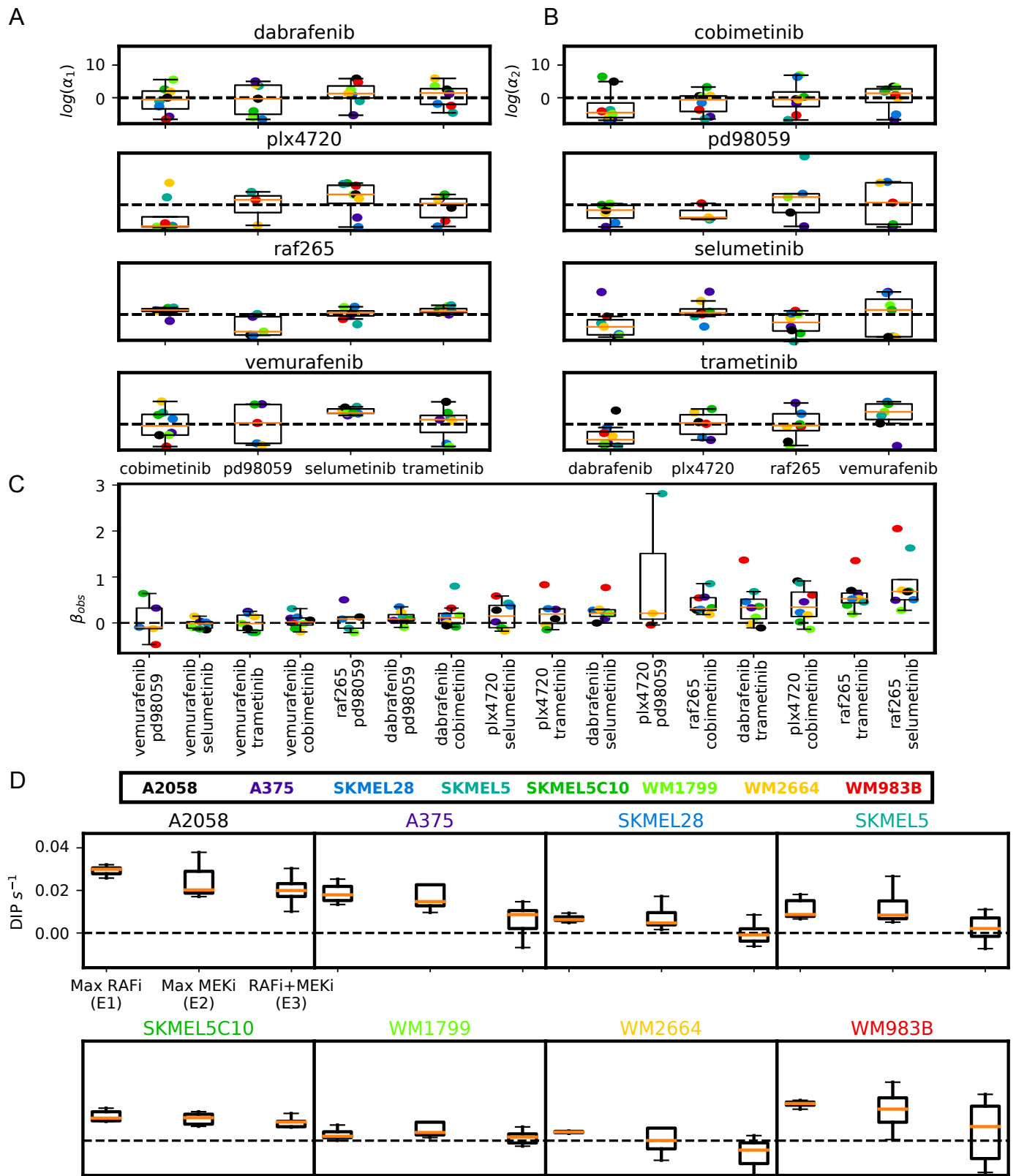


Figure S5

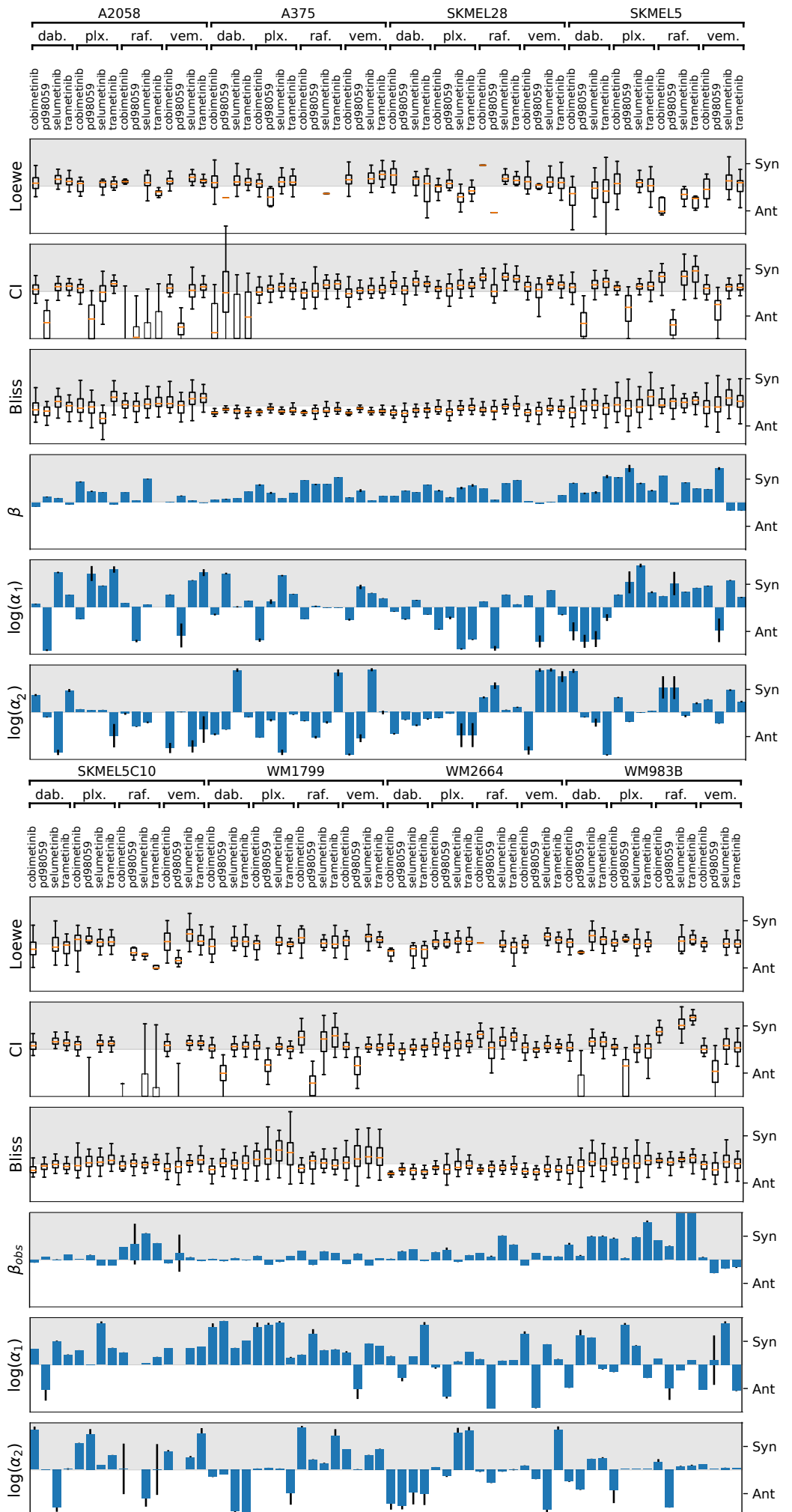


Figure S6

2 Supplemental Tables

Table S1: Annotation of parameters for the 2D Hill equation. Related to Figure 1, Figure S1.

U	Percent of unaffected cells
A_1, A_2	Percent of cells affected by drug 1 and drug 2, respectively.
$A_{1,2}$	Percent of cells affected by both drug 1 and drug 2.
d_1, d_2	Drug concentrations for drug pair
E_d	Measured DIP rate at (d_1, d_2)
C_1, C_2	EC_{50} for drugs 1 and 2 in isolation
r_x, r_{-x}	The forward and reverse transition rates between two states
h_1, h_2	Hill coefficients for dose response curves of drug 1 and 2 in isolation
E_0	The basal rate of proliferation in drug naive condition
E_1, E_2	E_{max} of drug 1 and 2 in isolation
E_3	E_{max} of the combination of drugs 1 and 2
α_1	Measure of how $[d_1]$ modulates the effective dose of $[d_2]$.
α_2	Measure of how $[d_2]$ modulates the effective dose of $[d_1]$.
β	Theoretical difference in maximal effect achievable with both drugs compared to the most efficacious drug alone.
β_{obs}	Observed difference in effect with both drugs at the maximum tested concentration as compared to either drug alone.

Table S2: Annotation of anti-cancer drugs used in NSCLC and BRAF-mutant melanoma screens with nominal target and target class. Related to Figure 2,3.

Class	Subclass	Drug	Tested Range	Nominal Target
NSCLC				
Epigenetic Regulators	BET	jq1	4.0uM-0.1nM,0nM	BET bromo-domain
	HDACi	abexinostat	0.3uM-0.8nM,0nM	HDAC
		entinostat	1.0uM-2.6nM,0nM	HDAC
		givinostat	10.0uM-41.1nM,0nM	HDAC
		m344	1.0uM-2.6nM,0nM	HDAC
		mocetinostat	0.3uM-0.8nM,0nM	HDAC
		panobinostat	0.4uM-0.0nM,0nM	HDAC
		pracinostat	10.0uM-41.1nM,0nM	HDAC
	TF	quisinostat	1.0uM-2.6nM,0nM	HDAC
		bazedoxifene	10.0uM-41.1nM,0nM	ER
Kinases	ALK	verteporfin	10.0uM-41.1nM,0nM	YAP
		ceritinib	4.0uM-0.1nM,0nM	ALK/IGF1R
	AURK/CDKs	ensartinib	4.0uM-0.1nM,0nM	ALK
		bml259	1.0uM-2.6nM,0nM	CDK
		zm447439	4.0uM-0.1nM,0nM	AURK
		dactolisib	4.0uM-0.1nM,0nM	PI3K/mTOR
	MAPK/PI3K	ly294002	10.0uM-41.1nM,0nM	PI3K
		rapamycin	0.3uM-0.8nM,0nM	mTOR
		sb253226	10.0uM-41.1nM,0nM	p38
		tak632	4.0uM-0.1nM,0nM	RAF
		trametinib	0.3uM-0.8nM,0nM	MEK
		u0126	10.0uM-41.1nM,0nM	MEK
Mitotic Checkpoint	SFK	ulixertinib	4.0uM-0.1nM,0nM	ERK
		bosutinib	10.0uM-41.1nM,0nM	Bcr-ABL/SFK
		dasatinib	1.0uM-3.9nM,0nM	SFK
		pp2	10.0uM-41.1nM,0nM	SFK
		quercetin	10.0uM-41.1nM,0nM	SFK
	DNA Syn/Dam	carmustine	10.0uM-41.1nM,0nM	DNA
		methotrexate	4.0uM-0.1nM,0nM	DHFR
		olaparib	20.0uM-0.3nM,0nM	PARP
		carfilzomib	4.0uM-0.1nM,0nM	Proteasome
		harringtonine	10.0uM-41.1nM,0nM	Ribosomes
Receptors & Channels	Protein Syn/Stab	mg132	4.0uM-0.1nM,0nM	Proteasome
		tanespimycin	4.0uM-0.1nM,0nM	HSP90
		cephalomannine	10.0uM-41.1nM,0nM	Microtubules
		docetaxel	0.3uM-0.8nM,0nM	Microtubules
		vindesine	0.3uM-0.8nM,0nM	Microtubules
	Tubulin	vinorelbinetartrate	10.0uM-41.1nM,0nM	Microtubules
		amiodarone	10.0uM-41.1nM,0nM	NA Channels
		bendroflume-thiazide	1.0uM-2.6nM,0nM	Cl channel
		cabozantinib	4.0uM-0.1nM,0nM	C-Met/Axl/Ret
		dronedarone	10.0uM-41.1nM,0nM	NA Channels
	Channels	ivacaftor	10.0uM-41.1nM,0nM	CFTR
		nateglinide	1.0uM-2.6nM,0nM	ATP-dependent K channels

BRAF-Mutant Melanoma	GPCRs	acetylcysteine aprepitant beclomethasone/dipropionate loratadine naftopidil nebivolol sp600125 thioridazine	10.0uM-41.1nM,0nM 10.0uM-41.1nM,0nM 1.0uM-2.6nM,0nM 10.0uM-41.1nM,0nM 10.0uM-41.1nM,0nM 10.0uM-41.1nM,0nM 10.0uM-41.1nM,0nM 10.0uM-41.1nM,0nM	Glutamate receptor Neuromedin receptor Glucocorticoid receptor
	MAPK-RTKIs	afatinib ag 879 gefitinib gsk1751853a gsk994854a gw458787a gw644007x gw694590a gw770249x linsitinib ponatinib tyrphostinag370	4.0uM-0.1nM,0nM 1.0uM-2.6nM,0nM 4.0uM-0.1nM,0nM 10.0uM-41.1nM,0nM 10.0uM-41.1nM,0nM 10.0uM-41.1nM,0nM 10.0uM-41.1nM,0nM 10.0uM-41.1nM,0nM 10.0uM-41.1nM,0nM 5.0uM-19.5nM,0nM 4.0uM-0.1nM,0nM 10.0uM-41.1nM,0nM	Histamine H1-receptors B1-adrenergic receptor B1 receptor JNK Adrenergic receptor EGFR/HER2 HER2/RAF-1 EGFR IGF1R/INSR IGF1R/INSR EGFR/ERBB4 Ret TIE2 FLT3 IGF1R FGFR PDGFRbeta
Kinases	MAPK/PI3K	dabrafenib plx4720 raf265 vemurafenib selumetinib trametinib pd98059 cobimetinib	0.4nM-0.39nM,0nM 8.0uM-7.8nM,0nM 1.0uM-3.9nM,0nM 8.0uM-7.8nM,0nM 4.0uM-61pM,0nM 0.4uM-6.1pM,0nM 0.4uM-6.1pM,0nM 0.8uM-12pM,0nM	BRAFV600 BRAFV600E & CRAF1 CRAF,BRAF, & BRAFV600E BRAFV600 MEK1 MEK1/2 MEK1 MEK1

Table S3: BRAFi sensitivity across CCLE BRAF-mutant melanoma cell line panel. Related to Figure 3.

CCLE Cell Line	DIP Rate (h^{-1}) at [8uM] PLX4270
A2058_SKIN	0.030
A375_SKIN	0.005
SKMEL28_SKIN	0.010
SKMEL5_SKIN	0.014
WM115_SKIN	0.013
WM1799_SKIN	-0.002
WM2664_SKIN	0.003
WM793_SKIN	0.015
WM88_SKIN	-0.020
WM983B_SKIN	0.021

Table S4: Differentially Expressed Genes (DEGs) between SKMEL5 subclones SC01, SC07, SC10 whose expression significantly correlated to BRAFi insensitivity (Pearson r) across panel of 10 cell-lines (expression data from Subramanian *et al.*). See Table S3 for quantification of sensitivity to BRAFi. Related to Figure 3.

Positive Correlation with BRAFi insensitivity			Negative Correlation with BRAFi insensitivity		
Gene symbol	r	p-value	Gene symbol	r	p-value
SLC7A11	0.816	0.004	GRIK3	-0.743	0.014
SLC16A7	0.807	0.005	PRELP	-0.720	0.019
TGFB1	0.666	0.036	CPVL	-0.684	0.029
NOX5	0.649	0.042	ITGA10	-0.659	0.038
LXN	0.646	0.044			

Table S5: Description of nested model tiers used in MCMC fit. Related to STAR Methods.

Model Tier	Fit Parameters	Approximations
#5	$\alpha_1, \alpha_2, E_3, E_1, E_2, C_1, C_2, h1, h2, E_0, r_1, r_2$	1. Rate of transition $(r_1, r_2) \gg 1$.
#4	$\alpha_2, E_3, E_1, E_2, C_1, C_2, h1, h2, E_0$	1. System obeys detail balance.
#3	$\alpha_2, E_3, E_1, E_2, C_1, C_2, h1, h2$	<ul style="list-style-type: none"> 1. All conditions tier 4 2. E_0 is the minimally observed effect.
#2	$\alpha_2, E_3, E_1, E_2, C_1, C_2$	<ul style="list-style-type: none"> 1. All conditions tiers 3,4 2. $h1, h2$ are from single drug fits or 1 if single fits failed converge.
#1	α_2, E_3, E_1, E_2	<ul style="list-style-type: none"> 1. All conditions tiers 2-4 2. C_1, C_2 are from single drug fits or the median concentration if single fits failed to converge.
#0	α_2, E_3	<ul style="list-style-type: none"> 1. All conditions tiers 1-4 2. E_1, E_2 are assumed to be the maximally observed effect maximum concentration of d_1 and d_2 respectively.